ABSTRACT

Title of thesis: DYNAMICS AND CONTROL OF AN
ELASTIC ROD IN AIR AND WATER

Travis Taylor Burch
Master's of Science, 2019

Thesis directed by: Professor Derek Paley
Department of Aerospace Engineering

This thesis investigates the modeling and control of bio-inspired flexible structures for robotics applications. Many animals move through complicated natural environments and perform complex tasks by exploiting soft structures. Soft structures are highly versatile and are a growing area of interest in robotics because they can have decreased weight, size, and mechanical complexity relative to more traditional rigid robotics. This work uses planar discrete elastic rod (PDER) theory for modeling two types of flexible structures. First, a flexible airfoil is modeled using PDER theory, including the Improved Lighthill model (ILM) of hydrodynamic forces to study the propulsion thrust. The propulsion thrust generated by rigid and flexible foils are also measured experimentally and compared to the model. Second, a state-space description of a flexible pendulum with torque input is presented. Linear state-and output-feedback hybrid controllers stabilize the inverted flexible pendulum starting from the down equilibrium.

DYNAMICS AND CONTROL OF AN ELASTIC ROD IN AIR AND WATER

by

Travis Taylor Burch

Thesis submitted to the Faculty of the Graduate School of the
University of Maryland, College Park in partial fulfillment
of the requirements for the degree of
Master's of Science
2019

Advisory Committee:
Professor Derek Paley, Chair/Advisor
Professor Alison Flatau
Professor Oliver Bauchau

Dedication

I would like to dedicate this thesis to Bill Watterson for his work on October 31, 1989.

Acknowledgments

First and foremost I would like to thank my advisor, Derek Paley for giving me the opportunity to work on challenging problems over the last two years. He is a talented and thoughtful researcher. I am fortunate to have had the opportunity to learn from him during my time as a student.

I would like to express my deepest gratitude towards Will Scott for his continued support through my time at Maryland. He has been a great aid in helping me to understand the research process, develop code used throughout the project, and work through tricky theoretical concepts.

A deep thanks are due to to Professors Oliver Bauchau, Allison Flatau, and Anya Jones for offering their time, expertise, and support throughout the duration of this work.

I would also like to thank Alyssa Novelia, and Oliver O'Reilly. I would not have been able to accomplish as much as I did using planar discrete elastic rod theory had it not been for their continued aid.

The support from by family, friends and lab-mates has been nothing short of extraordinary. My peers were a tremendous help academically and personally during the more stressful times of this endeavour.

It is impossible to remember all, and I apologize to those I've inadvertently left out.

Lastly, thank you all!

This research is supported by ARO Grant No. W911NF1610244

Table of Contents

List of Tables

List of Figures

List of Abbreviations

DER	Discrete Elastic Rods
PDER	Planar Discrete Elastic Rods
LAEBT	Large Amplitude Elongated Body Theory
ILM	Improved Lighthill model
AMM	Assumed Modes Method
CFD	Computation Fluid Dynamics
LQR	Linear Quadratic Regulator
RMS	Root mean squared

List of Nomenclature

$\bar{(\cdot)}$	Overbar refers to value in undeformed configuration
$(\cdot)^i$	Superscript index refers to an edge quantity
$(\cdot)_i$	Subscript index refers to a node quantity
$\breve{(\cdot)}$	Breve refers to a skew symmetric matrix
$\langle \boldsymbol{E}_1,\ \ \boldsymbol{E}_2,\ \ \boldsymbol{E}_3 \rangle$	Inertial frame basis vectors
$\boldsymbol{t}^i$	Tangent vector if the i^{th} edge
$\boldsymbol{n}^i$	Normal vector if the i^{th} edge
$\boldsymbol{e}^i$	The i^{th} edge
$\boldsymbol{x}_i$	The i^{th} node
N	The number of nodes
φ_i	The turning angle at the i^{th} node
κ_i	The curvature at the i^{th} node
$\bar{\kappa}_i$	The intrinsic curvature of the i^{th} node
g	The acceleration due to gravity
ρ	The density of the body
m_i	The mass of the i^{th} node
M	The node mass matrix
A_i	The cross-sectional area of the body cut at the i^{th} node
A^i	The cross-sectional area of the i^{th} edge
I^i	The moment of inertia of the i^{th} edge
I_i	The area moment of inertia of the i^{th} node
l^i	The length of the i^{th} edge
$\bar{l}^i$	The intrinsic length of the i^{th} edge
L_{tot}	Total length of the undeformed body
$\bar{\ell}_i$	The Voronoi region i^{th} node
ζ	Tuned numerical damping in PDER
E	Elastic modulus
E_t	Total mechanical energy
E_e	Total elastic energy
E_s	Total stretching energy
E_b	Total bending energy
E_g	Total gravitational potential
$\boldsymbol{F}_{s_i}$	Force due to stretching applied at the i^{th} node
$\boldsymbol{F}_{b_i}$	Force due to bending applied at the i^{th} node
$\boldsymbol{F}_{ext}$	Total external force applied to PDER
$\boldsymbol{q}$	State vector containing node positions
$\boldsymbol{v}$	State vector containing node velocities
$\boldsymbol{\theta}$	Angle of the edges relative to inertial the frame
$\dot{\boldsymbol{\theta}}$	Angular velocities of the edges relative to the inertial frame
$\boldsymbol{q}_{theta}$	Vector containing angle and angular velocities of the edges
$\boldsymbol{q}^*_{theta}$	The upright equilibrium point for an inverted pendulum

List of Nomenclature cont.

$\mathcal{I}$	The node inertia matrix in polar form
$\mathcal{C}$	The Coriolis and centrifugal moment vector in polar form
$\mathcal{V}$	The gravitational and bending moment vector in polar form
$\mathcal{F}$	The input moment vector in polar form
T	The input torque provided at the base of the inverted pendulum
T^*	The equilibrium input torque provided to the inverted pendulum
$\boldsymbol{z}$	The coordinates of the linearized inverted pendulum system
A	The dynamic matrix of the linearized inverted pendulum system
B	The input matrix of the linearized inverted pendulum system
C	The observation matrix of the linearized inverted pendulum system
A_b	Banded matrix representing the bending forces
A_g	Banded matrix representing the gravitational forces
K	The feedback control gain matrix
Q	State error cost weighting matrix
R	Input cost weighting matrix
Q_θ	Edge angle error cost weighting coefficients
$Q_{\dot{\theta}}$	Edge angular velocity error cost weighting coefficients
L	The observer feedback gain matrix
Q_n	Process noise covariance matrix
R_n	Measurement noise covariance matrix
ω	The frequency of the open-loop swing up input
$\mathcal{A}$	The amplitude of the open-loop swing up input
w_{crit}	The critical buckling width of a beam
$\boldsymbol{e}$	State error of linearized observer feedback system
$\boldsymbol{F}_{ext,j}$	Total external force on the j^{th} node
$\boldsymbol{F}^j_{ext}$	Total external force and moment on the j^{th} edge
$\boldsymbol{F}^j_{reac}$	Total reactive force on the j^{th} edge
$\boldsymbol{F}^j_{res}$	Total resistive force on the j^{th} edge
$\boldsymbol{f}^j_{ext}$	Total external force on the j^{th} edge
$\boldsymbol{c}^j_{ext}$	Total external moment on the j^{th} edge
$\boldsymbol{\eta}^j$	The velocity and angular velocity of the j^{th} edge
$\dot{\boldsymbol{\eta}}^j$	The acceleration and angular acceleration of the j^{th} edge
$\boldsymbol{V}^j$	The velocity of the j^{th} edge
$\boldsymbol{\Omega}^j$	The angular velocity of the j^{th} edge
$\mathcal{M}^j_{reac}$	The added mass tensor
$\bar{M}^j_f$	The added fluid mass tensor of the j^{th} edge
$\bar{I}^j_f$	The added fluid rotational inertia tensor of the j^{th} edge
$\boldsymbol{S}^j_f$	The first moment of inertia tensor of the j^{th} edge
AR	Aspect Ratio of the airfoil
h	Height of the airfoil

List of Nomenclature cont.

$\boldsymbol{\beta}_{reac}^{j}$	The Coriolis and centrifugal forces on the j^{th} edge
$\boldsymbol{\beta}_{reac}^{j-}$	The momentum flux and pressure forces on the left plane of the j^{th} edge
$\boldsymbol{\beta}_{reac}^{j+}$	The momentum flux and pressure forces on the right plane of the j^{th} edge
C_m	The added mass coefficient
C_f	The fluid friction coefficient
C_d	The fluid drag coefficient
C_1, C_2, C_3, C_4	The resistive model hydrodynamic coefficients
Ad_s	The adjoint map operator from the $j-1^{\text{th}}$ frame to the j^{th} frame

Chapter 1: Introduction

1.1 Motivation

Engineering is a continued effort to improve and optimize the performance of man-made designs that utilize an understanding of fundamental scientific principles. Over many millennia animals have been optimized to perform in their respective environments through natural pathways. Many animals move through complicated natural environments and perform complex tasks by exploiting soft structures. The overwhelming majority of the animal world is soft bodied, or comprised primarily of soft tissues and fluid [1]. Soft structures are highly versatile and are a growing area of interest in robotics. The use of soft structures could expedite the ability of robotics to interact with humans and perform medical tasks [1]. Robotic systems with flexible rather than rigid components have decreased weight, size, and mechanical complexity [2]. Flexible robots are used in soft gripping applications [3] as well as in underwater locomotion [4]. However, flexible systems are challenging to model because they may be highly nonlinear, have infinite degrees of freedom, and are generally described by partial differential equations [5]. This structural complexity, coupled with the complexity of interacting with dynamic environments, such as an ambient fluid, make the modeling and control of flexible manipulators a rich problem to be solved. Model-based design can be used to explore parameter space for performance where it would be difficult or expensive to vary parameters experimentally. Simplified models for fluid-structure interactions may help to shed light on optimal control and design characteristics for underwater robotics.

1.2 Relation to state of the art

Fluid-structure interactions are immensely important in underwater robotics. Existing literature such as [4] neglect the structural dynamics and chose to assume a shape approximated by a Joukowsky airfoil undergoing periodic oscillations in camber ratio. The resulting forces on the body are then obtained through the use of potential flow theory and vortex models. Additionally, numerical methods such as computational fluid dynamics (CFD) have been used to study the deformation and thrust production of flexible propulsors in [6]. Using CFD for closed loop control of an underwater fish is infeasible because of on-board computational power requirements and the time needed to obtain a solution. Experimental approaches have been used in [7] and [8] to determine the thrust production and propulsive efficiency of rigid and flexible pitching plates respectively. Fluid added mass is used in Quinn et al.'s [9] in connection with Euler-Bernoulli beam theory to experimentally investigate the mode shapes and thrust production of a heaving plate. This approach is closely connected with the large amplitude elongated body theory (LAEBT) developed by Lighthill in [10], where change in the momentum of the fluid control volume around the submerged body is used to calculate resultant fluid forces. This method is improved and reformulated by Porez et al. in [11] to be applied in robotic multibody systems. This work has implemented the Improved Lighthill model (ILM) from [11] to compare the predicted loads on a pitching rigid foil to experimental data. An attempt was made to implement the ILM for a flexible silicone rubber airfoil modeled as a planar discrete elastic rod (PDER), though further work must be done to properly model the fluid forces for use with the PDER framework.

In the field of flexible manipulators much of the existing literature focuses on relatively stiff structures with sufficiently well-defined vibration modes such that the Assumed Modes Method (AMM) [12] is a good approximation for the behavior of the system. However, existing models break down when soft materials such as silicone rubber undergo large deformations [12]. Nonetheless, state-space modeling and principled control design is possible using elastic rod theory [13].

As a representative problem to investigate control design, this work considers an inverted flexible pendulum with a torque input at the base. The nonlinear behavior and complexity of existing models that describe the dynamics of flexible beams make traditional control design complicated [14]. Prior work has been done in modeling inverted cantilever beams on carts with tip masses [15], [16]. In other work, [17], [18], [19], the pendulum is free to rotate at a pivot on a moving cart. Singla [20] models a cart-pole system as a series of two rigid rods linked by torsional springs. We will adapt the method from [20] and model a flexible pendulum as a series of six rigid rods linked by nonlinear torsional springs.

1.3 Contributions of thesis

This work is the first that I am aware of to apply the Improved Lighthill model of hydrodynamic forces to study the propulsion thrust of a flexible airfoil modeled using discrete elastic rods. Experiments are performed to measure the thrust produced by pitching rigid and flexible airfoils in water around the quarter chord at varying amplitudes and frequencies. Experiments suggest that higher thrust is achieved at higher frequencies and higher amplitudes for both the rigid and flexible airfoils. Validation of PDER numerical modeling is performed using a molded silicone rubber airfoil undergoing periodic deformations. The ILM is used to attempt to predict fluid forces on a rigid airfoil.

The contributions of the work on the flexible pendulum are (1) a state-space description of a flexible pendulum with torque input using planar discrete elastic rod theory; (2) a state-feedback hybrid control design for balancing the inverted flexible pendulum; (3) and a dynamic output-feedback hybrid control design using a linear observer that relies only on measurements of the position and angular velocity of the base of the rod. Performance is illustrated using numerical simulations of a PDER pendulum. The pendulum parameters are chosen to satisfy the conventional self-buckling condition; simulations suggest that the feedback control design balances some rods that buckle under zero input. To model the pendulum dynamics we employ a PDER formulation in state-space form [13]. We design a full-state feedback controller for the system linearized about the up equilibrium and apply that controller to the full nonlinear system. Additionally, an open-loop swing-up controller is implemented using the natural frequency of a rigid pendulum of the same length. We design a linear observer using a standard Kalman filter design and stabilize the up equilibrium using observer-based feedback with measurements collected only at the base of the pendulum.

1.4 Outline of thesis

Chapter 2 presents background and notation for planar discrete elastic rods and briefly presents the background for Lighthill's large amplitude elongated body theory as well as Porez et al.'s Improved Lighthill model. Chapter 3 presents the experimental platform and procedure used to compare the thrust generation potential of a flexible vs rigid airfoil. Chapter 4 presents the linearized model and state feedback control design for stabilizing a flexible inverted pendulum then extends the framework to include and output feedback control design. Chapter 5 summarizes the results and future work.

Chapter 2: Modeling of structural and fluid forces

2.1 Planar Discrete Elastic Rods

This chapter will provide the background for planar discrete elastic rod (PDER) theory, drawing heavily from the work done by Jawed et al. [21]. First, the discretization scheme and notation will be introduced. The next sections will describe the physical parameters of the rod. Finally, the energies pertaining to the rod and the forces arising from the elastic energies are described.

An elastic rod is a continuum structure with an infinite number of degrees of freedom [16]. In order to characterize the behavior of a rod we utilize a discrete model. The behavior of the elastic rod is suitably approximated using a planar discrete elastic rod formulation [13], which is a specialization of three-dimensional discrete elastic rod theory [22].

A rod is discretized into a series of N nodes and $N-1$ edges as shown in Fig. 2.1. The greater the number of nodes, the more closely the PDER agrees with analytical models [21].

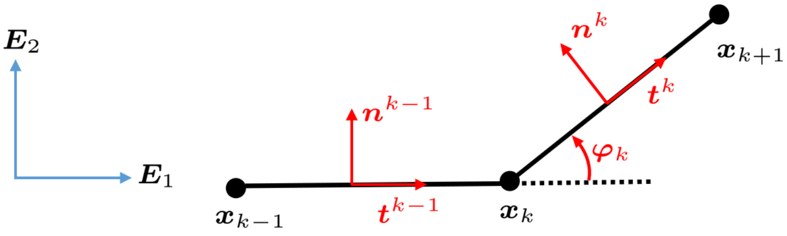

Figure 2.1: Notation for labeling edges and nodes [13]

2.1.1 Kinematics

The position vector of each node is given in the inertial frame where the i^{th} node is located at

$$\boldsymbol{x}_i = x_i \boldsymbol{E}_1 + y_i \boldsymbol{E}_2, \tag{2.1}$$

where x_i and y_i are Cartesian coordinates, $\boldsymbol{E}_1$ is a unit vector in the horizontal direction, and $\boldsymbol{E}_2$ is a unit vector in the vertical direction. It follows that $\boldsymbol{E}_3 = \boldsymbol{E}_1 \times \boldsymbol{E}_2$ is directed out of the plane. Edge $\boldsymbol{e}^i$ connects nodes $\boldsymbol{x}_i$ and $\boldsymbol{x}_{i+1}$. (Note, edges are denoted with superscript indexing and nodes are denoted by subscript indexing.) An edge is defined in [13] as

$$\boldsymbol{e}^i = \boldsymbol{x}_{i+1} - \boldsymbol{x}_i, \quad \boldsymbol{t}^i = \frac{\boldsymbol{e}^i}{\|\boldsymbol{e}^i\|}, \text{ and } \boldsymbol{n}^i = \boldsymbol{E}_3 \times \boldsymbol{t}^i. \tag{2.2}$$

where the vectors $\boldsymbol{t}^i$ and $\boldsymbol{n}^i$ are the unit tangent and unit normal of the i^{th} edge, respectively, given in the inertial frame. The relative orientation of edges is defined by their turning angle φ_i, which can also be represented as curvature κ_i, [13] i.e.,

$$\begin{gathered} \varphi_i = \cos^{-1}\left(\boldsymbol{t}^{i-1} \cdot \boldsymbol{t}^i\right) \\ \kappa_i = \frac{\ell_i}{R_i} = 2\tan\left(\frac{\varphi_i}{2}\right), \end{gathered} \tag{2.3}$$

for $i = 2, \ldots, N-1$

where $\ell_i = \frac{1}{2}(\|\boldsymbol{e}^{i-1}\| + \|\boldsymbol{e}^i\|)$ is the length of the Voronoi region of the i^{th} node and $R_i = \frac{\ell_i}{2}\cot(\frac{\varphi_i}{2})$ is the radius of the osculating circle seen in Fig. 2.2.

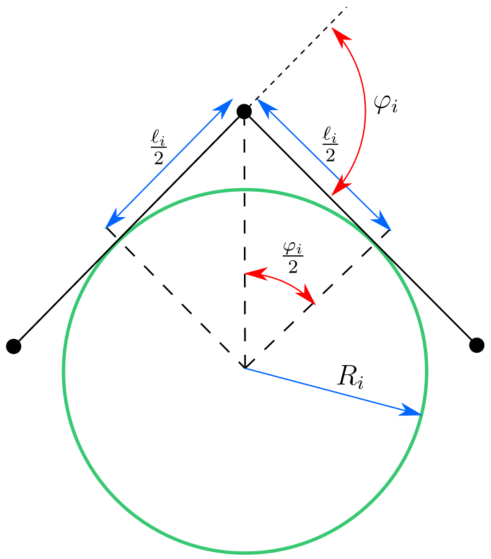

Figure 2.2: Osculating circle of radius $R_i = \frac{\ell_i}{2}\cot(\frac{\varphi_i}{2})$ is tangent to two lines of length ℓ_i and represents the discrete approximation for curvature of continuous rod [21].

2.1.2 Physical parameterization

The undeformed shape of a PDER is defined by the set of intrinsic lengths $\bar{l}^i$ of each edge and intrinsic curvatures $\bar{\kappa}_i$ at nodes $i = 2, \ldots, N-1$. Following Bergou et al. [22], the i^{th} edge has a mass m^i defined by the volume integral over the region of the body represented by that edge.

$$m^i = \int\int\int \rho(s_1, s_2, s_3)\ ds_1 ds_2 ds_3, \quad i = 1, \ldots, N-1 \tag{2.4}$$

where s_1, s_2, and s_3 are the body frame coordinates of each edge. The mass associated with the i^{th} node, m_i, is the average mass of the edges meeting at this node, i.e.,

$$\begin{aligned} m_1 &= \frac{1}{2}m^1 \\ m_i &= \frac{1}{2}\left(m^i + m^{i-1}\right), \quad i = 2, \ldots, N-1 \\ m_N &= \frac{1}{2}m^{N-1}. \end{aligned} \tag{2.5}$$

The node mass matrix M takes the form

$$M = \begin{bmatrix} m_1 & 0 & \dots & 0 & 0 \\ 0 & m_1 & \dots & 0 & 0 \\ \vdots & \vdots & \ddots & \vdots & \vdots \\ 0 & 0 & \dots & m_N & 0 \\ 0 & 0 & \dots & 0 & m_N \end{bmatrix}. \tag{2.6}$$

The cross sectional area of an edge is given by A^i where

$$A^i = \frac{1}{2}(A_i + A_{i+1}) \tag{2.7}$$

and A_i is the cross sectional area of the undeformed body cut at the i^{th} node. The moment of inertia across the i^{th} edge is defined by the volume integral in Eq. (2.8) where the s_1, s_2, s_3 are the body frame coordinates that corresponds to the tangent, normal, and out of plane directions respectively.

$$I^i = \frac{1}{m^i} \int\int\int \rho(s_1, s_2, s_3) s_2^2 \; ds_1 ds_2 ds_3, \quad i = 1, \dots, N-1 \tag{2.8}$$

The area moment of inertia of the i^{th} node is based on the average area moment of inertia between the edges meeting at that node [13].

$$I_i = \frac{1}{2}\left(I^i + I^{i-1}\right) \tag{2.9}$$

2.1.3 Energies and Forces

The PDER dynamics incorporate the various forms of potential energy within the system as follows. The curvature κ_k determines the bending energy E_b. The change in length of each edge determines the stretching energy E_s. These two energies, bending and stretching, combine to form the elastic energy E_e. The elastic energy together with the gravitational potential energy E_g is the total potential energy E_t [13] : i.e.,

$$\begin{aligned} E_e &= E_s + E_b \\ E_t &= E_e + E_g, \end{aligned} \tag{2.10}$$

where [13]

$$\begin{aligned} E_s &= \frac{1}{2}\sum_{k=1}^{N-1} EA^k \left(\frac{\|\boldsymbol{e}^k\|}{\|\bar{\boldsymbol{e}}^k\|} - 1\right)^2 \|\bar{\boldsymbol{e}}^k\| \\ E_b &= \frac{1}{2}\sum_{j=2}^{N-1} \frac{EI_j}{\bar{\ell}_j}(\kappa_j - \bar{\kappa}_j)^2 \\ E_g &= g\sum_{i=1}^{N} m_i y_i \end{aligned} \tag{2.11}$$

and E is the elastic modulus of the pendulum, A^k is the average cross-sectional area of the k^{th} edge, I_j is the area moment of inertia of the j^{th} node, and $\bar{\ell}_j = \frac{1}{2}(\|\bar{l}^j\| + \|\bar{l}^{j-1}\|)$ is the undeformed length of the Voronoi region of the j^{th} node.

2.1.3.1 Stretching energy

The stretching energy arises from strain along the tangent vector of an edge. We can express stretching force acting on each node as the sum of the partial derivatives of the stretching energy with respect to each connected edge.

$$\begin{aligned}
\boldsymbol{F}_{s_1} &= \frac{\partial E_s}{\partial \boldsymbol{e}^1} = EA^1\left(\frac{\|\boldsymbol{e}^1\|}{\|\bar{\boldsymbol{e}}^1\|} - 1\right)\boldsymbol{t}^1, \\
\boldsymbol{F}_{s_j} &= -\frac{\partial E_s}{\partial \boldsymbol{e}^{j-1}} + \frac{\partial E_s}{\partial \boldsymbol{e}^j} \\
&= -EA^{j-1}\left(\frac{\|\mathbf{e}^{j-1}\|}{\|\bar{\mathbf{e}}^{j-1}\|} - 1\right)\boldsymbol{t}^{j-1} + EA^j\left(\frac{\|\mathbf{e}^j\|}{\|\bar{\mathbf{e}}^j\|} - 1\right)\mathbf{t}^j, \\
\boldsymbol{F}_{s_N} &= -\frac{\partial E_s}{\partial \boldsymbol{e}^{N-1}} = -EA^{N-1}\left(\frac{\|\boldsymbol{e}^{N-1}\|}{\|\boldsymbol{e}^{\bar{N}-1}\|} - 1\right)\boldsymbol{t}^{N-1}
\end{aligned} \tag{2.12}$$

The first and last node are only subject to the forces from one edge, while the internal nodes are subject to the forces of the preceding and prior edges.

2.1.3.2 Bending energy

The bending energy arises from rotational strain illustrated by a difference between the intrinsic and current curvature. We can express bending force acting on each node as a sum of the partial derivatives of the bending energy with respect to each connected edge.

$$\begin{aligned}
\boldsymbol{F}_{b_1} &= \frac{\partial E_b}{\partial \boldsymbol{e}^1}, \\
\boldsymbol{F}_{b_i} &= -\frac{\partial E_b}{\partial \boldsymbol{e}^{i-1}} + \frac{\partial E_b}{\partial \boldsymbol{e}^i}, \\
\boldsymbol{F}_{b_N} &= -\frac{\partial E_b}{\partial \boldsymbol{e}^{N-1}},
\end{aligned} \tag{2.13}$$

where

$$\begin{aligned}
\frac{\partial E_b}{\partial \boldsymbol{e}^k} =& \frac{EI_{k_2}}{\bar{\ell}_k}\left[\left(\kappa_k - \bar{\kappa}_k\right)\frac{\partial \kappa_k}{\partial \boldsymbol{e}^k}\right]\dots \\
&+ \frac{EI_{k+1_2}}{\bar{\ell}_{k+1}}\left[\left(\kappa_{k+1} - \bar{\kappa}_{k+1}\right)\frac{\partial \kappa_{k+1}}{\partial \boldsymbol{e}^k}\right].
\end{aligned} \tag{2.14}$$

We note that Eq. (2.14) depends on the partial derivatives of the curvature with respect to the edge where those partial derivatives are given by

$$\begin{aligned}\frac{\partial \kappa_{k+1}}{\partial \boldsymbol{e}^k} &= -\frac{2}{l^k(1+\boldsymbol{t}^k\cdot\boldsymbol{t}^{k+1})}\boldsymbol{n}^k,\\ \frac{\partial \kappa_{k}}{\partial \boldsymbol{e}^k} &= \frac{2}{l^k(1+\boldsymbol{t}^{k-1}\cdot\boldsymbol{t}^{k})}\boldsymbol{n}^k.\end{aligned} \tag{2.15}$$

Due to the fact that curvature is defined by the turning angle between two edges, the bending force applied at the i^{th} node is determined by the relative positions of the four edges, $\boldsymbol{e}^{i-2}$ through $\boldsymbol{e}^{i+1}$.

This PDER formulation is a useful tool to characterize the behavior of highly flexible structure. The discrete nature of this formulation provides a simple and intuitive method for principled control design. This formulation is versatile and can be simply coupled with other discrete models.

2.2 Improved Lighthill model

This section will begin by providing the background for the Improved Lighthill model (ILM), drawing heavily from the work done by Porez et al. [11]. We will also discuss the backwards Euler numerical integration method used to solve the equations of motion.

Lighthill is responsible for developing the large-amplitude elongated-body theory (LAEBT) which calculates the forces acting on submerged bodies undergoing fish-like swimming [10]. The fluid around the fish, or in this case an airfoil, can be considered inviscid due to the high Reynolds numbers involved in fish-like swimming [11]. This assumption means that the fluid can only exert pressure forces, i.e. there is no shearing stress. However, as in [11], we include the modeling of viscous forces through a Taylor-like resistive model from [23]. In LAEBT, thrust is generated via deformations in body shape over time that accelerate fluid along the body until it is shed into the wake at the caudal fin, i.e. the trailing edge [24].

In the ILM there are two types of hydrodynamic forces: reactive and resistive. Reactive forces are exerted by the acceleration of the fluid around the submerged body. Resistive forces are exerted by the viscous stresses applied at the boundary layer of the submerged body.

Following from PDER, in this work the submerged body is discretized into N nodes and $N-1$ edges as in Fig. 2.1. The total external hydrodynamic force exerted on the j^{th} edge is the sum of the reactive and resistive forces [25].

$$\boldsymbol{F}^j_{ext} = \boldsymbol{F}^j_{reac} + \boldsymbol{F}^j_{res} \tag{2.16}$$

where $\boldsymbol{F}^j_{ext} = \begin{pmatrix} \boldsymbol{f}^{jT}_{ext} & \boldsymbol{c}^{jT}_{ext} \end{pmatrix}^T$ is a (6×1) vector containing the forces and moments acting on the j^{th} edge. $\boldsymbol{F}^j_{reac}$ and $\boldsymbol{F}^j_{res}$ are (6×1) vectors containing the forces and moments from the reactive and resistive forces respectively. The state vector in this formulation of LAEBT, developed by [11], stores the translational and rotational velocities of each edge and is given as

$$\boldsymbol{\eta}^j = \begin{pmatrix} \boldsymbol{V}^j \\ \boldsymbol{\Omega}^j \end{pmatrix} \tag{2.17}$$

where $\boldsymbol{\eta}^j$ is a (6×1) vector containing the inertial velocity expressed in the body frame of the j^{th} link. $\boldsymbol{V}^j$ and $\boldsymbol{\Omega}^j$ are the translational and rotational velocities respectively. The translational velocity of the j^{th} edge is the velocity of the j^{th} node.

In order to make this formulation of the fluid forces compatible with the PDER state space, the forces on the edge are split in half and applied to the two nodes that comprise the edge. The torque is converted into a pair of equal and opposite forces that act along parallel lines of action.

$$
\begin{aligned}
\boldsymbol{F}_{ext,1} &= \frac{1}{2}\boldsymbol{f}^{1}_{ext} - \frac{1}{l^{1}}\boldsymbol{n}^{1}\boldsymbol{c}^{1}_{Z} \\
\boldsymbol{F}_{ext,j} &= \frac{1}{2}\left(\boldsymbol{f}^{j}_{ext} + \boldsymbol{f}^{j-1}_{ext}\right) - \frac{1}{l^{j}}\boldsymbol{n}^{j}\boldsymbol{c}^{j}_{Z} + \frac{1}{l^{j-1}}\boldsymbol{n}^{j-1}\boldsymbol{c}^{j-1}_{Z}, \quad i = 2, \ldots, N-1 \\
\boldsymbol{F}_{ext,N} &= \frac{1}{2}\boldsymbol{f}^{N-1}_{ext} + \frac{1}{l^{N-1}}\boldsymbol{n}^{N-1}\boldsymbol{c}^{N-1}_{Z}
\end{aligned}
\tag{2.18}
$$

where $\boldsymbol{c}^{j}_{Z}$ is the moment acting on the j^{th} edge in the E_3 direction. This expression is then rotated into the inertial frame and used in the backwards Euler integration scheme.

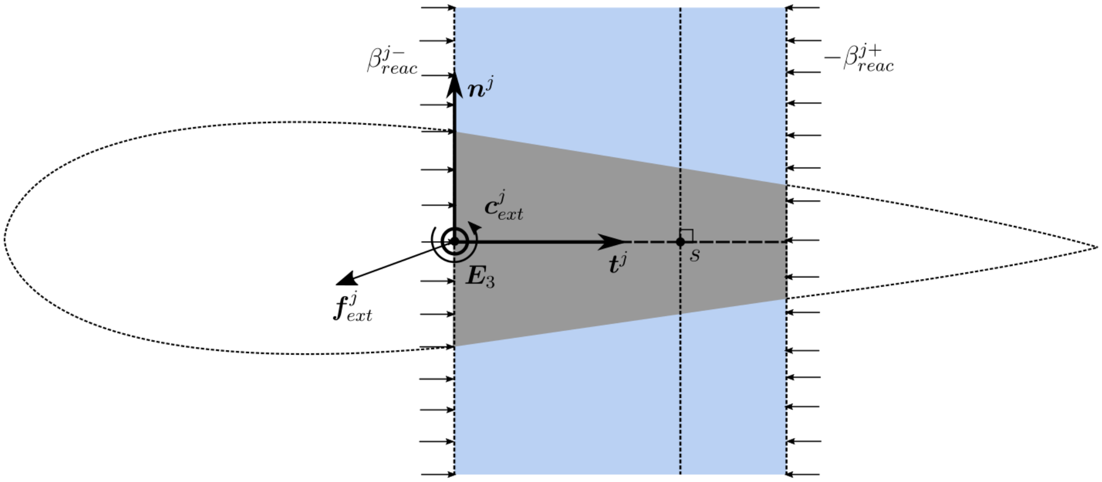

Figure 2.3: Control volume of the j^{th} body.

2.2.1 Reactive forces

The reactive force on an edge is calculated by determining the change in momentum of the control volume of fluid that surrounds that edge as seen in Fig. 2.3. This includes the acceleration of the fluid contained in the control volume as well as the fluid pressure acting along the surface of the control volume. The reactive force is given by Eq. (2.19)

$$\boldsymbol{F}^j_{reac} = -\mathcal{M}^j_{reac}\dot{\boldsymbol{\eta}}^j - \boldsymbol{\beta}^j_{reac} - \boldsymbol{\beta}^{j-}_{reac} - \boldsymbol{\beta}^{j+}_{reac} \tag{2.19}$$

where $\mathcal{M}^j_{reac}$ is the added mass tensor, and the $\boldsymbol{\beta}^j_{reac}$ terms are the combination of the flux of fluid momentum and the pressure forces exerted at the boundary of each control volume. The added mass tensor is given by Eq. (2.20)

$$\begin{gathered}\mathcal{M}^j_{reac} = \begin{pmatrix} M^j_f & -\breve{\boldsymbol{S}}^j_f \\ \breve{\boldsymbol{S}}^j_f & I^j_f \end{pmatrix} = \begin{pmatrix} l^j \bar{M}^j_f & -\frac{l^{j2}}{2}\bar{M}^j_f \breve{\boldsymbol{t}}^j \\ \frac{l^{j2}}{2}\bar{M}^j_f \breve{\boldsymbol{t}}^j & \frac{l^{j3}}{3}\breve{\boldsymbol{t}}^{jT}\bar{M}^j_f \breve{\boldsymbol{t}}^j + l^j \bar{I}^j_f \end{pmatrix} \\ \bar{M}^j_f = \frac{C_m \rho_f \pi h^2}{4}(\boldsymbol{n}^j {\boldsymbol{n}^j}^T) \ ; \qquad \bar{I}^j_f = 0_{3\times3}\end{gathered} \tag{2.20}$$

Here the $\breve{(\cdot)}$ operator denotes a skew symmetric matrix such that $(\breve{\boldsymbol{a}})\boldsymbol{b} = \boldsymbol{a} \times \boldsymbol{b}$, l^j is the length of segment, ρ_f is the fluid density, $C_m = 0.5$ is a dimensionless shape coefficient, h is the height of the segment in the E_3 direction, t_j and n_j are the tangent and normal vectors respectively. The reactive forces produced by the added mass accelerated by the Coriolis and centrifugal accelerations are given by

$$\beta^j_{reac} = \begin{pmatrix} -\hat{\boldsymbol{\Omega}}^j(\breve{\boldsymbol{S}}^j_f \boldsymbol{\Omega}^j) + \breve{\boldsymbol{\Omega}}^j(\bar{M}^j_f \boldsymbol{V}^j) \\ \breve{\boldsymbol{\Omega}}^j(I^j_f \boldsymbol{\Omega}^j) + \breve{\boldsymbol{S}}^j_f(\breve{\boldsymbol{\Omega}}^j \boldsymbol{V}^j) \end{pmatrix} + \begin{pmatrix} 0_{3\times1} \\ \breve{\boldsymbol{V}}^j(\bar{M}^j_f \boldsymbol{V}^j) \end{pmatrix}. \tag{2.21}$$

The boundary effects that account for the pressure on the control volume as well as the flux of momentum through the control volume is given by

$$\beta^{j-}_{reac} = -\begin{pmatrix} (\bar{M}^j_f \boldsymbol{V}^j){\boldsymbol{t}^j}^T \boldsymbol{V}^j \\ 0_{3\times1} \end{pmatrix}(0) + \frac{1}{2}\begin{pmatrix} (\boldsymbol{V}^{jT}\bar{M}^j_f \boldsymbol{V}^j + \boldsymbol{\Omega}^{jT}\bar{I}^j_f \boldsymbol{\Omega}^j)(0)\boldsymbol{t}^j \\ 0_{3\times1} \end{pmatrix} \tag{2.22}$$

and

$$\beta^{j+}_{reac} = Ad^T_{l^j}\left[\begin{pmatrix}(\bar{M}^j_f \boldsymbol{V}^j)\boldsymbol{t}^{j^T}\boldsymbol{V}^j \\ \\ 0_{3\times 1}\end{pmatrix}(l^j) - \frac{1}{2}\begin{pmatrix}(\boldsymbol{V}^{jT}\bar{M}^j_f\boldsymbol{V}^j + \boldsymbol{\Omega}^{jT}\bar{I}^j_f\boldsymbol{\Omega}^j)(l^j)\boldsymbol{t}^j \\ \\ 0_{3\times 1}\end{pmatrix}\right] \tag{2.23}$$

where

$$Ad^T_s = \begin{pmatrix}1_{3\times 3} & 0_{3\times 3} \\ \\ s\check{\boldsymbol{t}}^j & 1_{3\times 3}\end{pmatrix} \tag{2.24}$$

2.2.2 Resisitive forces

The ILM developed by Porez et. al. [11] includes the viscous forces through a Taylor-like resistive model from [23]. The resistive force is characterized by four constants. These constants, $C_1 = C_f\rho_f P$, $C_2 = C_d\rho_f h$, $C_3 = 0$, $C_4 = 0$ are empirically determined constants from [26]. Here C_f and C_d are dimensionless coefficients relating to friction and drag respectively, ρ_f is the fluid density, P is the average cross section perimeter, and h is the height of the submerged body. The resistive hydrodynamic forces are parameterized by C_f and C_d. The resistive force on the j^{th} edge is given by Eq. (2.25)

$$F^j_{res} = \frac{1}{2}\int_0^{l^j} Ad^T_s \begin{pmatrix}(C_1 V^j_X|V^j_X|)\boldsymbol{t}^j + (C_2 V^j_Y|V^j_Y|)n_j + (C_3 V^j_Z|V^j_Z|)b_j \\ (C_4|\Omega^j_X|\Omega^j_X)\boldsymbol{t}^j\end{pmatrix} ds \tag{2.25}$$

As in [11], C_3 and C_4 are forced to zero because the motion of the airfoil is assumed to be planar.

2.3 Numerical integration method

This is a non-trivial problem to solve numerically due to the implicit nature of the coupling between the fluid forces and structural deformations. The PDER model is solved in parallel using a backwards Euler scheme to improve numerical stability. The approximations are propagated through

$$\frac{d\boldsymbol{z}}{dt} = f(\boldsymbol{z}, t), \quad \boldsymbol{z}(i+1) = \boldsymbol{z}(i) + \Delta t f(\boldsymbol{z}(i+1), t + \Delta t) \tag{2.26}$$

where $\boldsymbol{z}$ is an arbitrary state vector and Δt is the time step. The block diagram for the integration scheme is shown in Fig. 2.4. In practice, the node positions, velocities and the forces on each node are solved for simultaneously using `fsolve()` in Matlab. Using this integration scheme we are able to easily compute the constraining forces.

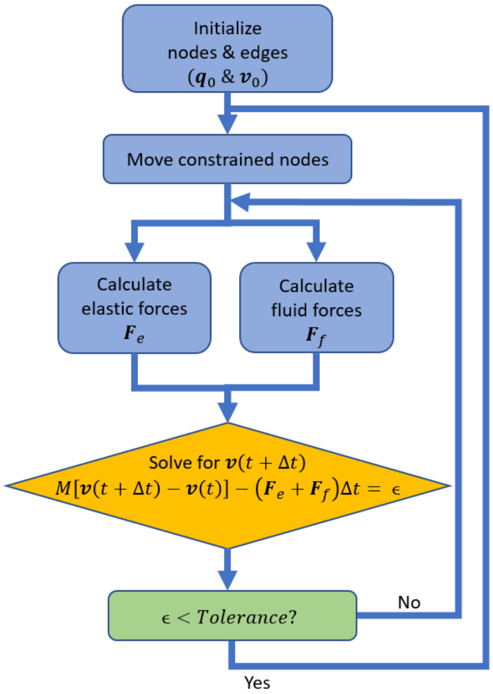

Figure 2.4: Block diagram showing the backwards Euler scheme used to solve the system of equations implicitly. The fluid forces are assumed to be zero in air.

Chapter 3: Experimental thrust of rigid and flexible pitching airfoils

This chapter aims to compare the thrust generation ability between a rigid and flexible airfoil in water. The chapter will discuss the experimental setup, procedure, and results of oscillating a rigid and flexible airfoil in water to generate thrust. We will then compare the experimental data to the thrust calculated by the Improved Lighthill model (ILM) and discuss the results.

3.1 Experimental setup

The respective airfoil is fabricated around MakerBeam supports such that the airfoil is being actuated around its quarter chord. The two supports in each airfoil are spaced at 20 mm. Each airfoil is actuated using a Savox SV-0235MG servo being powered at 12 volts. The servo is controlled using an Arduino Uno which communicates serially with Matlab. The servo chassis is suspended by two TAL221 load cells, which are being read using a National Instruments NI SCC-68 board and a National Instruments NI USB-6225 data acquisition system. A schematic of the experimental setup can be seen in Figs. 3.1 and 3.2.

Each airfoil is submerged in a cross section of a flow tank made by Loligo Systems with variable flow speed. The cross section of the flow tank measures 25×25 cm. To avoid surface effects of the fluid, the airfoil is submerged 3 cm below the surface of the water. High contrast visual markers were placed evenly spaced at 20 mm increments along the bottom side of the submerged airfoil as seen in Fig. 3.3. Images of the bottom of the airfoil

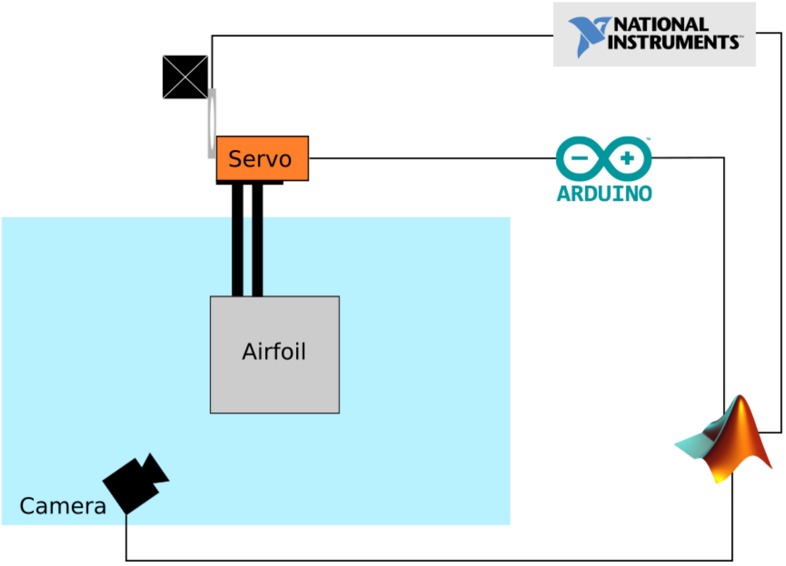

Figure 3.1: Experimental Schematic showing the load cells suspending the servo and airfoil from a rigid support. The camera is attached to the bottom of the flow tank and views the bottom of the airfoil. The load cells are read using a National Instruments board and the servo is controlled via an Arduino Uno. The National Instruments board, Arduino Uno and underwater camera all interface with Matlab.

Figure 3.2: Experimental setup showing the viewing angle of the underwater camera and and the suction cup mount used to attach it to the flow tank. The servo chassis and load cell array are shown mounted to a rigid beam with the airfoil attached to the control arm of the servo.

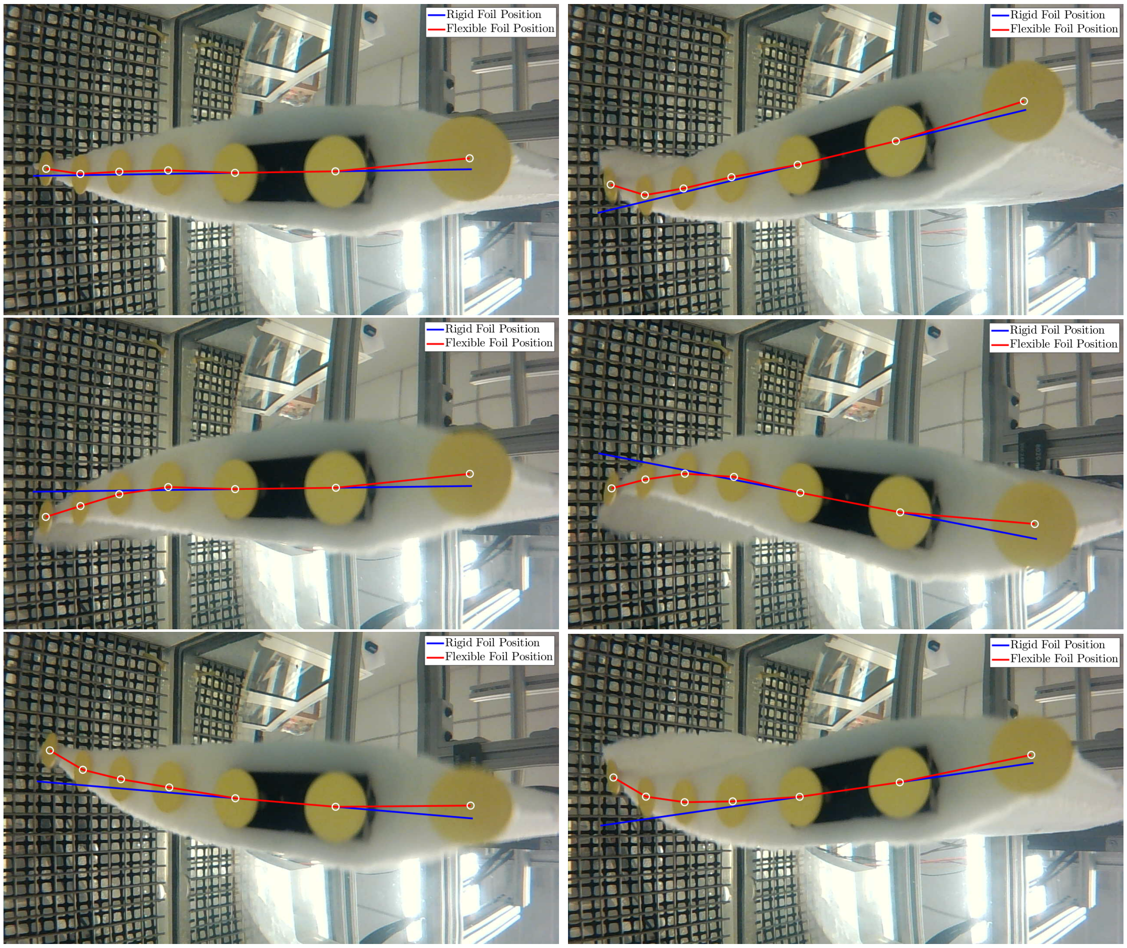

Figure 3.3: Sequential images of deformed flexible airfoil in water (read from left to right). The white circles show the position of the centroid of the markers, which are identified via computer vision. The red line shows the midline of the flexible airfoil. The blue line shows the overlay of the midline of a rigid foil at the same servo command angle.

were collected by a submerged camera. The camera being used was an IceCap REEF-cam with a resolution of 720p (1280 × 720) using 0.9 effective mega pixels. The images were collected at a frame rate of 30 frames per second. The camera was affixed to the bottom of the flow tank and angled up to view the bottom of the airfoil. Due to the limited size of the flow tank the camera took images of the airfoil at an angle. This angle was corrected for using the computer vision Matlab toolbox and the Single Camera Calibrator app in Matlab. Calibration is done to obtain intrinsic and extrinsic parameters that correct for lens distortion and localize the position of the camera respectively. From calibration, the mean reprojection error of the corrected images is 1.43 pixels as can be seen in Fig. 3.4. Additional information on camera calibration can be found in appendix A.

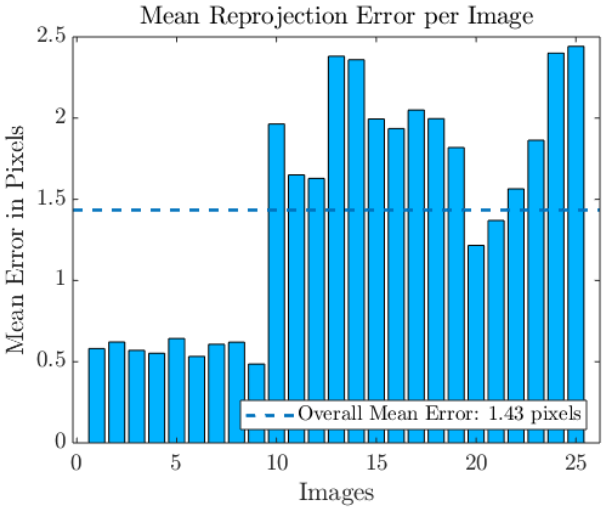

Figure 3.4: Reprojection Error of calibration images. The mean reprojection error of the corrected images is 1.43 pixels. Images taken at at an angle and images taken near the edges of the field of view of the camera result in larger reprojection errors

3.2 Discretization of airfoil using planar discrete elastic rod theory

The airfoil is modeled as a planar discrete elastic rod (PDER) where the midline of the airfoil takes the form of a series of nodes and edges with $N = 8$. The cross sectional area corresponding to the node is based on the profile of the airfoil. We assume a naturally straight rod with an intrinsic curvature, $\bar{\kappa}_i = 0$ at all nodes. The nodes are evenly spaced with intrinsic edge lengths of $\bar{l}^i = 20$ mm for all edges. The third node, $\boldsymbol{x}_3$, is fixed at the origin and edge $\boldsymbol{e}^3$, rotates about the fixed node at a fixed radius. The input to the airfoil is a prescribed rotation of the edge, $\boldsymbol{e}^3$. A silicone rubber airfoil was cast for experimentation, the measurements of the profile of the airfoil were taken every 20 mm and are provided in Table 3.1. The height of the airfoil is $h = 115$ mm and has an aspect ratio of $AR = \frac{\text{Height}}{\text{Length}} = 0.82$.

Table 3.1: Airfoil parameters measured every 20 mm from nose to tail

Index j	1 (Nose)	2	3	4	5	6	7	8 (Tail)
X-Position [mm]	0	20	40	60	80	100	120	140
Width [mm]	0	18.5	18.5	16.8	13.4	9.9	3.6	0
A_j [mm^2]	0	2133.0	2133.0	1933.0	1544.0	1144.0	414.0	0
I_j [mm$^4 \times 10^6$]	0	802	802	601	305	123	5.91	0

The cross sectional area used in calculations is the cross sectional area of the slice at the corresponding node. The mass of each edge is found while the airfoil is undeformed by assuming constant density and approximating the shape of the airfoil between two nodes as a trapezoidal prism (see Fig. 2.3). The elastic modulus is chosen as a tuning parameter for the PDER because of the inherent uncertainty in the elastic modulus of highly flexible materials. The stress/strain relationship of silicone-rubber is nonlinear [27], though as we will show in Sec. 3.4, assuming a linear stress/strain relationship near 0% elongation provides agreement between the model and experimental data. The flexural stiffness, EI is compared to the measured flexural stiffness of a sunfish [28] in Fig. 3.5

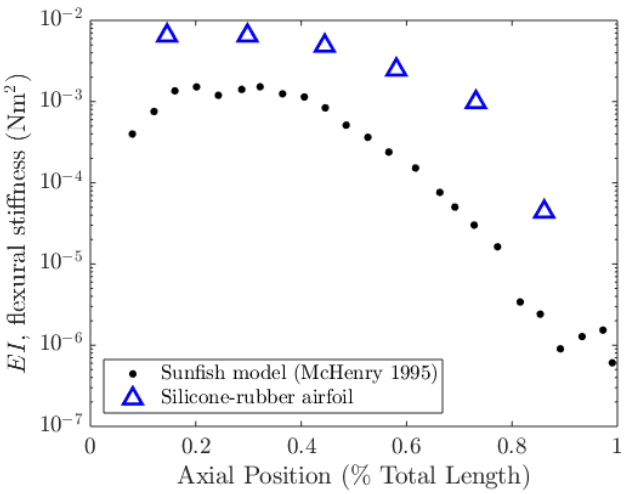

Figure 3.5: Comparison between flexural stiffness of silicone-rubber airfoil to sunfish model [28]

3.3 Experimental methods

This section details the methods used for data collection. Calibration was performed for the two load cells which suspend the servo and for the underwater camera used for computer vision. We also describe the testing procedure and analyze the results obtained from experimentation.

3.3.1 Load cell calibration

The load cells used in the experimental test bed are TAL221 load cells. The load cells attached to the chassis above the flow tank were then calibrated by applying a known load to the mid-height of the airfoil. The obtained load cell calibration curve is shown in Fig. 3.6. It is assumed that by summing the load cell signals only the thrust force is measured, i.e. that the force applied transverse to the airfoil is not coupled with the thrust measurement. Taking the difference of the load cell signals provides the signal that contains the torque applied to the body and the transverse force, though these signals are coupled. This coupling can be seen in the illustration in Fig. 3.7.

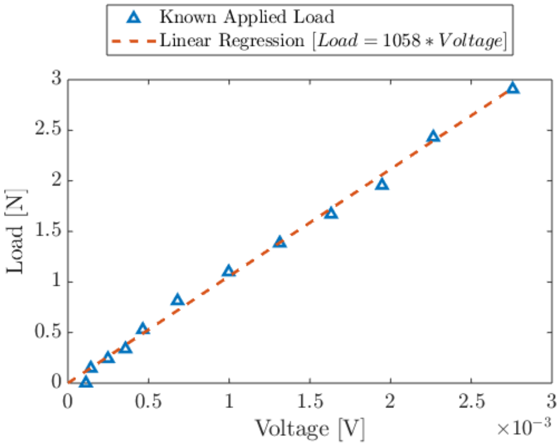

Figure 3.6: Load cell calibration curve showing the known applied known applied loads against voltage. A linear fit is used to determine the calibration coefficient of 1058 $[\frac{N}{V}]$

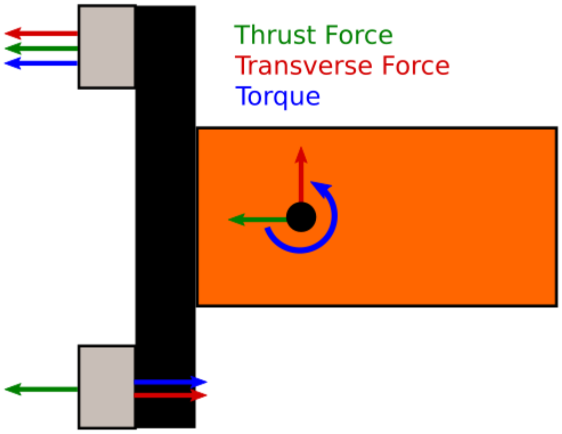

Figure 3.7: The components of the loads being measured by each load cell. Summing the signals provides only the thrust measurement while differencing the signals provides the torque and transverse force (coupled).

3.3.2 Data collection routine

Experiments are performed at frequencies ranging from 0.5 Hz to 2 Hz at 0.5 Hz increments, and amplitudes from 4 degrees to 10 degrees at increments of 2 degrees. The tests are performed with an ambient flow speed of 5 $\mathrm{cm\,s^{-1}}$, corresponding to $Re \approx 6900$. The servo is controlled via an Arduino Uno with an internal timing circuit and the National Instruments data acquisition system collects data at 300 Hz. To synchronize the timestamps of the Arduino, the National Instruments data acquisition system, and the images collected by the underwater camera, each device communicates serially with Matlab. The automated procedure for collecting and synchronizing data can be seen in Algorithm 1 in appendix B. Before the test is performed a manual calibration of the camera extrinsic parameters is performed. Additional information on camera calibration can be found in appendix A. The marker positions are extracted from the images collected during the experiment and converted into real world coordinates using the computer vision toolbox in Matlab.

3.4 Experimental results

This sections discusses the results of the validation the PDER model using a flexible airfoil in air, then analyzes the experimental and predicted hydrodynamic forces on a rigid foil. Finally, we discuss the propulsion thrust produced by a flexible airfoil in water.

3.4.1 Flexible airfoil in air

The first of the experiments is performed with the flow tank drained of water such that the airfoil is suspended in the air. This is done as a validation of the PDER model structural model where only forces arising from structural deformations are simulated, i.e the without fluid forces. The position of the airfoil is measured in each of the experiments using computer vision. Using `fminsearch()` the simulation is fit to experimental data with the numerical damping, ζ, and elastic modulus, E as tuning parameters. The curve fitting routine was driven by reducing the cost function Eq. (3.1)

$$J = \sum_{j=1}^{N_{exp}} \sqrt{\sum_{i=1}^{N} (\boldsymbol{y}_{meas,i,j} - \boldsymbol{y}_{sim,i,j})^T (\boldsymbol{y}_{meas,i,j} - \boldsymbol{y}_{sim,i,j})} \tag{3.1}$$

where N_{exp} is the total number of experiments in the test matrix, $\boldsymbol{y}_{meas,i}$ and $\boldsymbol{y}_{sim,i}$ are the y-position of the i^{th} node through time measured in the experiment and in simulation respectively. The fitting parameters were found to be: $E = 8.1112$ MPa and $\zeta = 0.1238$. The agreement between the experimental and simulated node position agree very well and an example can be seen in Fig. 3.8. The root-mean squared (RMS) error per measurement for each test case can be seen in Fig. 3.9. We note that the error is minimized at a low frequency and low amplitude and that error increases with both frequency and amplitude.

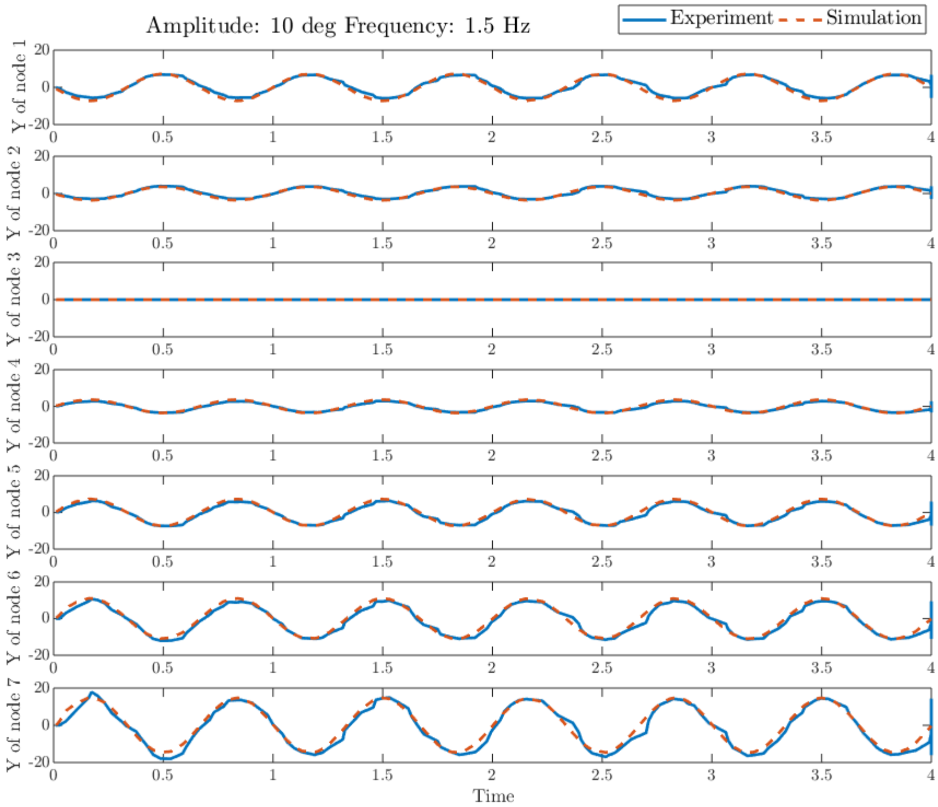

Figure 3.8: Time series for one of the points in parameter space (Amplitude: 10 deg Frequency: 1.5 Hz) comparing the experimental and simulated position of flexible airfoil in air for the best case tuning parameters.

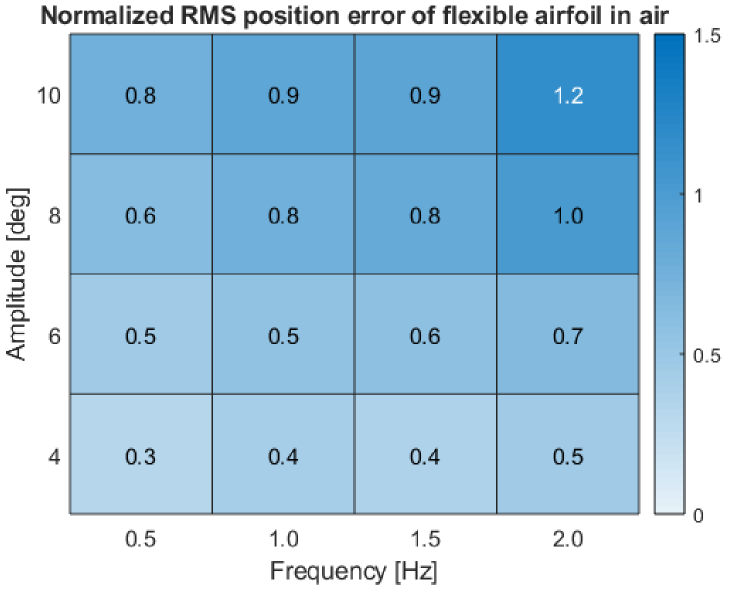

Figure 3.9: Heatmap of RMS position error per measurement (30 Hz) for the flexible airfoil in air. Model and experimental data agree most at low frequencies and amplitudes.

3.4.2 Rigid airfoil in water

The rigid foil is actuated with a sinusoidally changing angle. The thrust force is measured for each test condition. The signal from the load cell array is filtered using a band-stop filter designed in Matlab using the `designfilt()` function. An infinite impulse response band-stop filter is designed with two stop bands. The first stop band is from 6 to 8 Hz and the second is from 50 to 60 Hz; these ranges correspond to the oscillations arising from the experimental test bed. The thrust is approximately sinusoidal where the net offset corresponds to the average thrust. We note from Fig. 3.11 that the thrust generated by oscillating the rigid foil in water is approximately sinusoidal with a frequency of 2 times the driving frequency. The peak in thrust occurs twice over the course of one oscillation as the airfoil is briefly parallel with the E_1 direction (where phase $= 0,\ \pi,\ 2\pi$).

It is possible to solve for the fluid forces on the rigid foil analytically by the ILM. The resulting prediction of the thrust is shown plotted against the thrust measured experimentally in Fig. 3.11 where the thrust is sinusoidal with a frequency of double the driving frequency. The peaks in thrust predicted by the model are phase shifted $\frac{\pi}{2}$ from the experimental data and the maximum thrust predicted by the model occurs when the foil is at the maximum angle, i.e. when the angular acceleration is greatest (phase $= \frac{\pi}{2},\ \frac{3\pi}{2}$). The ILM does not show good agreement with experimental data, as the curves are $\frac{\pi}{2}$ out of phase with one another and the amplitude of the curves are different in magnitude.

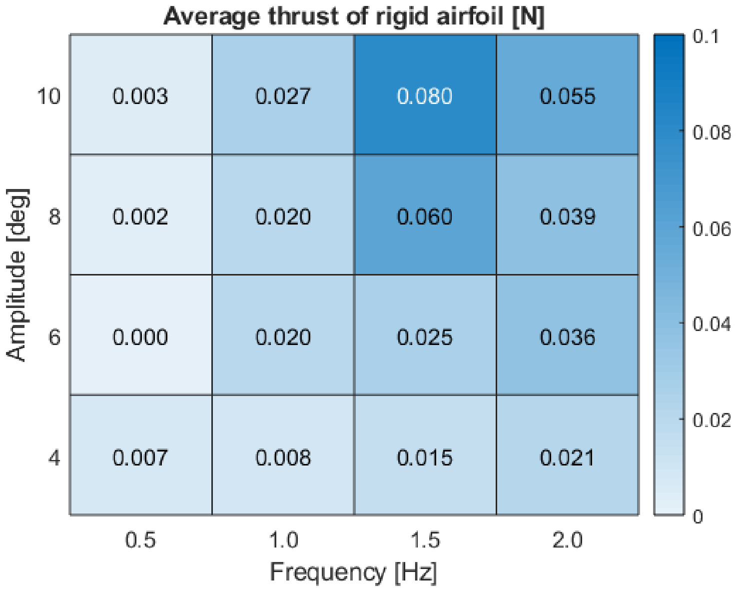

Amplitude [deg]	0.5	1.0	1.5	2.0
10	0.003	0.027	0.080	0.055
8	0.002	0.020	0.060	0.039
6	0.000	0.020	0.025	0.036
4	0.007	0.008	0.015	0.021

Figure 3.10: Heatmap showing the thrust produced by a rigid foil (in newtons) for frequencies ranging from 0.5 to 2 Hz and amplitudes ranging from 4 to 10 degrees. The maximum thrust observed in experiments is generated using an amplitude of 10 degrees and a frequency of 1.5 Hz

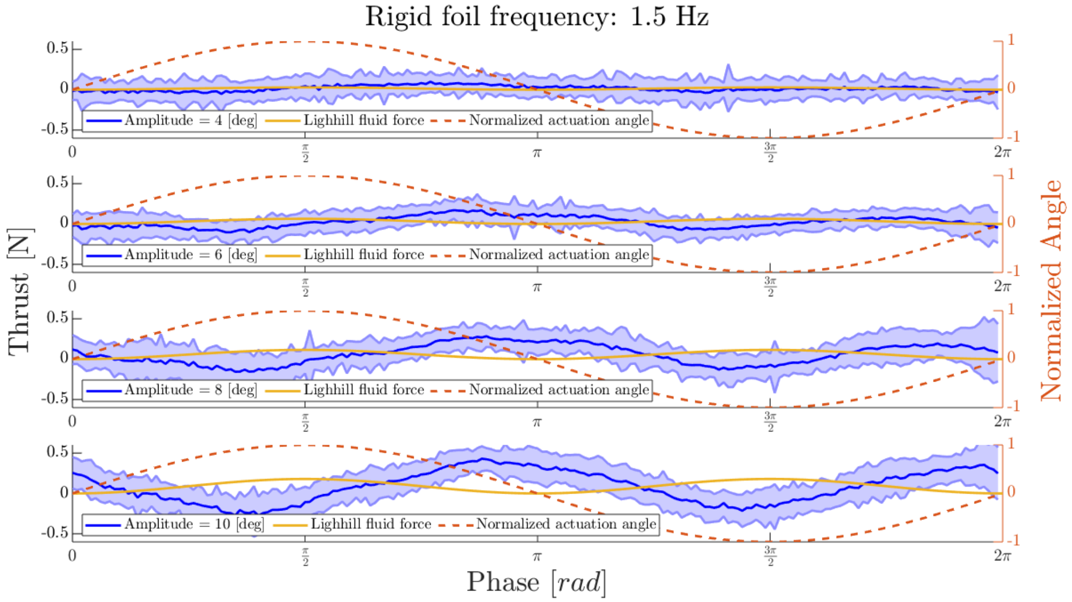

Figure 3.11: Rigid airfoil phase averaged thrust measured for amplitudes 4-10 deg at a frequency of 1.5 Hz. The thrust is approximately sinusoidal with maximums at phase = 0, π, 2π. The shading around the blue curve shows the 2σ error bounds for the phase averaged thrust. The yellow curve shows the fluid force predicted from the ILM given the prescribed rigid body motion.

3.4.3 Flexible airfoil in water

After testing the rigid airfoil, we transition to performing experiments at the same frequencies and amplitudes from Sec. 3.3.2 for a flexible foil. The flexible foil is actuated with a sinusoidally changing angle. The thrust force is again measured for each test condition. The signal from the load cell array is filtered using a band-stop filter designed in Matlab using the `designfilt()` function. An infinite impulse response band-stop filter is designed with two stop bands. The first stop band is from 6 to 8 Hz and the second is from 50 to 60 Hz; these ranges correspond to the oscillations arising from the experimental test bed. The thrust is approximately sinusoidal with a net offset that corresponds to the average thrust. We can see in Fig. 3.13 the flexible airfoil has significantly lower amplitude oscillations in thrust than the rigid airfoil. Again, the thrust is approximately sinusoidal where the net offset corresponds to the average thrust. We again note that the thrust generated by oscillating the rigid foil in water is approximately sinusoidal with a frequency of 2 times the driving frequency. The peak in thrust occurs twice over the course of one oscillation as the airfoil is briefly parallel with the E_1 direction (where phase $= 0,\ \pi,\ 2\pi$).

The predicted fluid forces on the flexible foil are calculated using the ILM with the position data measured using computer vision (as seen in Fig. 3.3). The resulting prediction of the thrust is shown plotted against the thrust measured experimentally in Fig. 3.13 where the predicted thrust is approximately sinusoidal with a frequency of double the driving frequency. As in the rigid foil case, the peaks in thrust predicted by the model are phase shifted $\frac{\pi}{2}$ from the experimental data and the maximum thrust predicted by the model occurs when the foil is at the maximum angle (phase $= \frac{\pi}{2},\ \frac{3\pi}{2}$). For both the rigid and flexible foil, the model does not provide good agreement with the experimental data.

In both cases the curves are $\frac{\pi}{2}$ out of phase with one another and the amplitude of the curves are different in magnitude.

While thrust produced by a rigid airfoil experiences much higher amplitudes than that of a flexible airfoil, the flexible airfoil produces a greater amount of average thrust than the rigid airfoil. The average thrust produced by the rigid and flexible airfoils can be seen in Figs. 3.10 and 3.12 respectively. Fig. 3.14 shows the percent increase in average thrust generated by a flexible airfoil compared to a rigid airfoil. This trend may also be seen in Fig. 3.15 which plots the coefficient of thrust, C_T, against the Strouhal number, St. The coefficient of thrust and Strouhal number are given by

$$C_T = \frac{Thrust}{\frac{1}{2}\rho_f U_\infty^2 L_{tot} h}, \qquad St = \frac{fW}{U_\infty} \tag{3.2}$$

where U_∞ is the ambient flow speed, and W is the width of the wake (assumed to be the peak to peak amplitude of the trailing edge). Fig. 3.15 shows that for a given Strouhal number, the flexible foil used in experimentation will produce more thrust than a rigid foil of the same geometry.

3.5 Discussion

This chapter presented the experimental setup, procedure and results of oscillating a rigid and flexible airfoil in water to generate thrust. This experimental thrust was then compared to the thrust calculated by the ILM. Neither the thrust generated by the rigid airfoil or flexible airfoil (as measured experimentally) shows good agreement to the thrust calculated by the ILM. The maximum experimental thrust is phase shifted by $\frac{\pi}{2}$ from the maximum thrust predicted using the ILM. This disagreement between experimental data and the ILM may be explained because one of the core mechanisms of thrust production in LAEBT and subsequently the ILM is the acceleration of fluid along the length of a submerged body. The geometry (namely the aspect ratio) of the airfoil used in this work may not have allowed for an adequate amount of attached flow which accelerates the fluid along the length of the airfoil and into the wake. Additionally, the summation of the signals from the load cells may contain coupling between the thrust and transverse force that was summed to be zero.

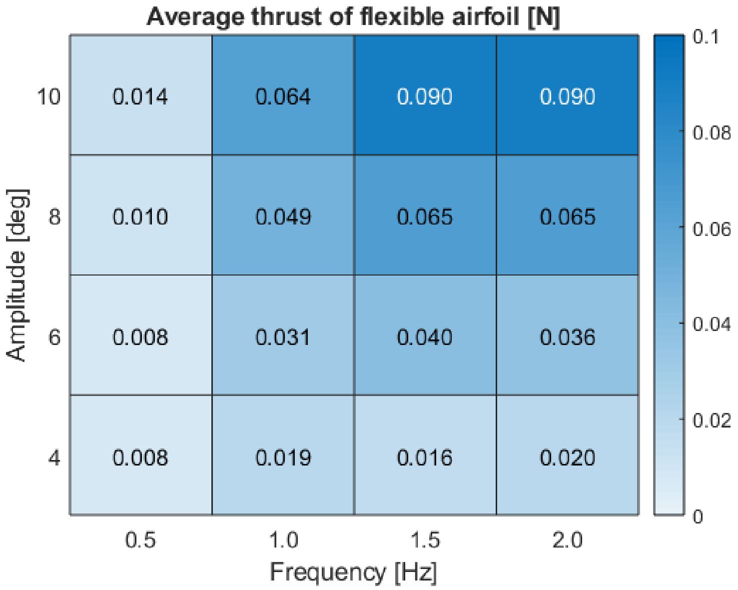

Figure 3.12: Heatmap showing the thrust produced by a flexible foil (in newtons) for frequencies ranging from 0.5 to 2 Hz and amplitudes ranging from 4 to 10 degrees. The maximum thrust observed in experiments is generated using an amplitude of 10 degrees and a frequency of 1.5 Hz

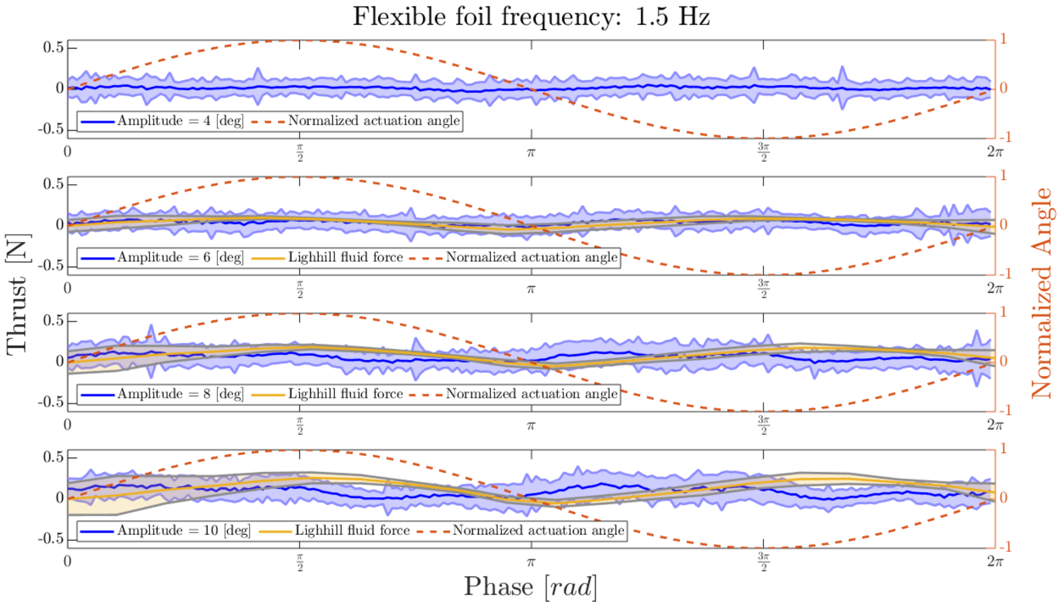

Figure 3.13: Flexible airfoil phase averaged thrust measured for amplitudes 4-10 deg at a frequency of 1.5 Hz. The thrust is approximately sinusoidal with maximums at phase = 0, π, 2π. The shading around the blue curve shows the 2σ error bounds for the phase averaged thrust. The yellow curve shows the fluid force predicted from the ILM given the measured structural deformations. The yellow shading shows the 2σ error bounds for the ILM fluid force. Lighthill fluid force omitted for amplitude of 4 degrees.

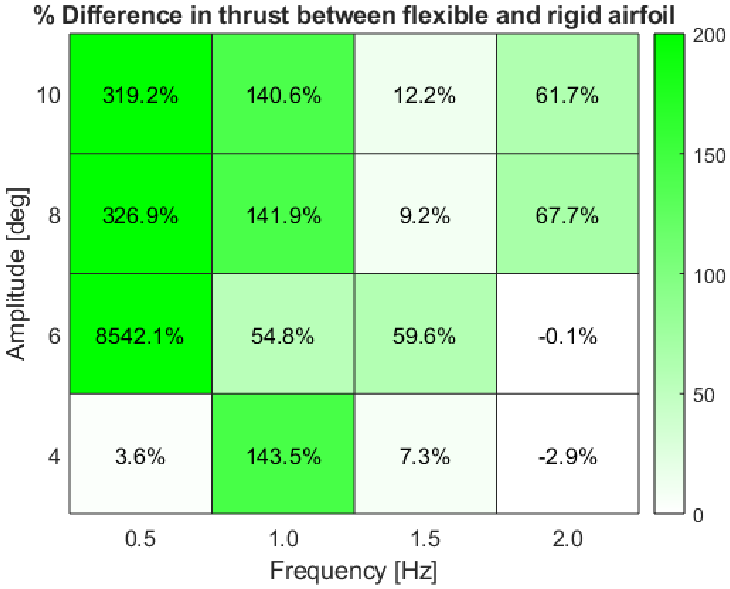

Figure 3.14: Heatmap shows the percent increase in thrust generated by a flexible foil over a rigid foil with the same geometry, amplitude and frequency. The greatest improvement appears at low frequencies, where the rigid foil produces nearly zero thrust.

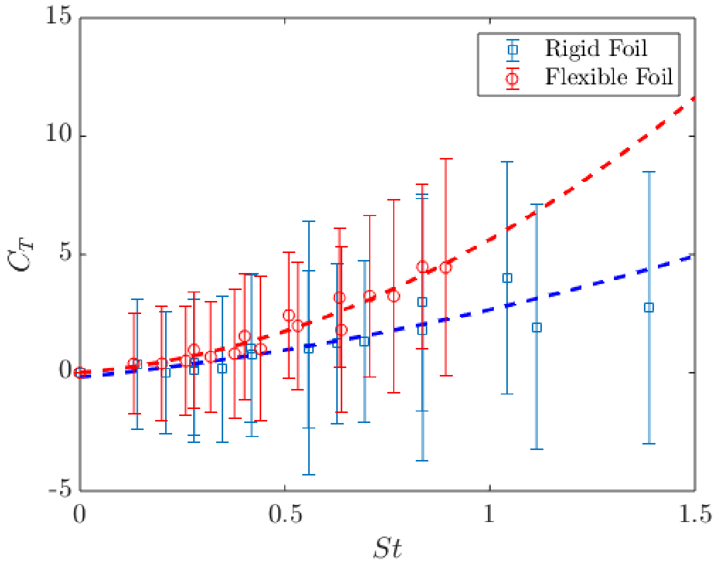

Figure 3.15: Coefficient of thrust against Strouhal number for a rigid foil and flexible foil. The ambient flow is 5 cm s^{-1} corresponding to $Re \approx 6900$. The plot suggests that thrust increases with Strouhal number, and that for an equal Strouhal number, the flexible foil produces more thrust.

Chapter 4: Feedback control of inverted elastic pendulum

As a method of exploring the control strategies that might be applied to flexible robotics, we first turn to the classic problem of the inverted pendulum. The flexible system is highly nonlinear and poses a challenge to traditional control strategies. For this work we will assume a naturally straight rod with an intrinsic curvature, $\bar{\kappa}_i = 0$ at all nodes. The nodes will be evenly spaced with intrinsic edge lengths of $\bar{l}^i = l$ for all edges. The control input will be a torque applied to the base of the pendulum.

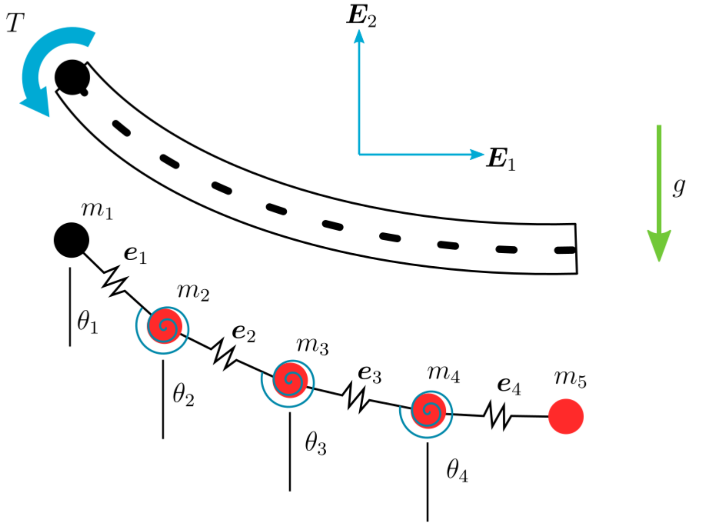

Figure 4.1: The PDER model of a flexible pendulum represents a continuous rod using discrete edges and nodes. Edges are modeled as linear elastic springs and nodes are modeled as nonlinear elastic torsional springs. The input to the system is a torque at the base of the pendulum.

4.1 State-space modeling of a planar discrete elastic rod

To write the pendulum dynamics in state-space form, let the state vector $\boldsymbol{q} = [x_1 \quad y_1 \quad \dots \quad x_N \quad y_N]^T$ represent the Cartesian coordinates of all of the nodes. The state-space model of the PDER is [13]

$$\begin{aligned}\dot{\boldsymbol{q}} &= \boldsymbol{v} \\ \dot{\boldsymbol{v}} &= -M^{-1}\left(\frac{\partial E_t}{\partial \boldsymbol{q}} + \zeta \boldsymbol{v} + \boldsymbol{F}_{ext}\right) \\ &= -M^{-1}\left(\left(\frac{\partial E_e}{\partial \boldsymbol{e}^{i+1}} - \frac{\partial E_e}{\partial \boldsymbol{e}^{i}}\right) + \frac{\partial E_g}{\partial \boldsymbol{q}} + \zeta \boldsymbol{v} + \boldsymbol{F}_{ext}\right)\end{aligned} \tag{4.1}$$

where $\boldsymbol{F}_{ext}$ is the column matrix containing the components of all external forces acting on the nodes and ζ is a damping coefficient. For the pendulum with node 1 fixed in place, the only external forces are the forces of constraint acting at node 1 and the force at node 2 that produce the input torque. The stretching, bending, and gravitational forces at each node are conservative and arise from the partial derivative with respect to $\boldsymbol{q}$ of the corresponding potential energy as can be seen in Sec. 2.1.3

We simulate the PDER equations of motion numerically with a backwards Euler scheme and the parameter values listed in Table 4.1. Fig. 4.2 shows the pendulum being released from horizontal initial conditions and allowed to swing freely without input. Note that with time step $\Delta t = 1 \times 10^{-4}$ there is minimal numerical damping and the total energy system is conserved.

4.2 State feedback hybrid control design

This section presents a hybrid controller that consists of a linear feedback controller near the up equilibrium and an open-loop swing-up controller. The design of the linear

Table 4.1: PDER pendulum simulation parameters

Name	Parameter	Value	Units
# of nodes	N	7	[ ]
Time step size	Δt	1×10^{-4}	[s]
Gravitational accel.	g	-9.81	$[\frac{\mathrm{m}}{\mathrm{s}^2}]$
Total length	L_{tot}	0.3	[m]
Rod width	w	$0.007 - 0.009$	[m]
Density	ρ	1.5×10^3	$[\frac{\mathrm{kg}}{\mathrm{m}^3}]$
Elastic Modulus	E	1.0×10^7	[Pa]
Stretching stiffness	EA	4.9×10^2	[N]
Bending stiffness	EI	2.0×10^{-3}	$[\mathrm{Nm}^2]$

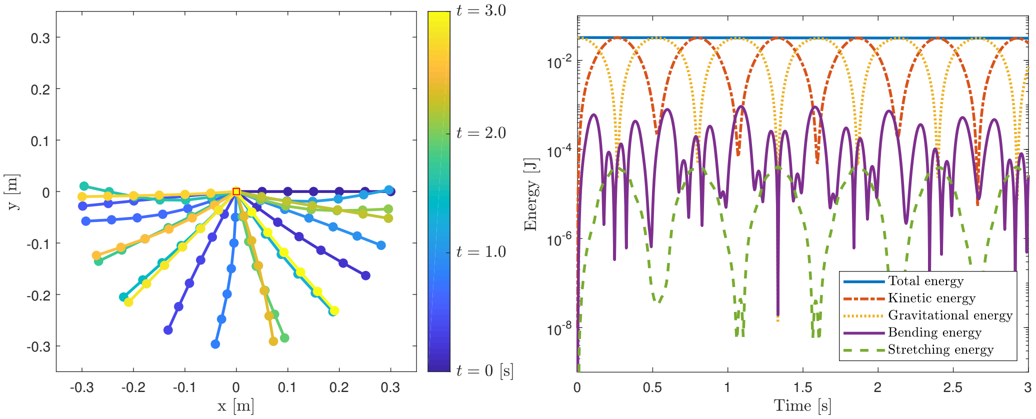

Figure 4.2: Open-loop simulation of a rod with $w = 0.7$ [cm] and time step $\Delta t = 1 \times 10^{-4}$ [s] under zero input, starting from rest at horizontal initial angle.

controller uses a PDER state-space representation of an inextensible, flexible pendulum. Simulation results show the swing up and stability behavior of the controlled system for rods above and below the self-buckling criterion.

4.2.1 Inextensible pendulum state-space form

Although the PDER model provides a suitable approximation to the elastic rod, for the design of a controller we have opted to further simplify the model as a multi-link pendulum with inextensible links and nonlinear torsional springs at the nodes. The edge length of the multi-link pendulum is constant, i.e., $\|\boldsymbol{e}^i\| = \|\bar{\boldsymbol{e}}^i\| = l^i$, where l^i is the length of the i^{th} link. The equations of motion for the inextensible pendulum model are found using the PDER potential energy Eq. (2.10), neglecting the stretching energy, which is one or more orders of magnitude smaller than the bending energy (see Fig. 4.2).

The simplified equations of motion for the elastic pendulum follow a recursive pattern that allows the equations to be written for any number of nodes. However, the equations in Cartesian coordinates quickly become very cumbersome, which hampers the ability to manipulate them symbolically. Therefore, the rigid-link pendulum model is derived with polar coordinates. In order to convert from the PDER state vector $(\boldsymbol{q}, \boldsymbol{v})$ to the state vector used in the sequel define $\boldsymbol{\theta} = \left[\theta_1, \ldots, \theta_{N-1}\right]^T$ and $\dot{\boldsymbol{\theta}} = \left[\dot{\theta}_1, \ldots, \dot{\theta}_{N-1}\right]^T$, where

$$\begin{aligned} \theta_i &= \tan^{-1}\left(\frac{-y_i + y_{i-1}}{x_i - x_{i-1}}\right), \\ \dot{\theta}_i &= \frac{\dot{x}_i - \dot{x}_{i-1}}{\|\boldsymbol{e}_i\|}\cos\theta_i + \frac{\dot{y}_i - \dot{y}_{i-1}}{\|\boldsymbol{e}_i\|}\sin\theta_i, \end{aligned} \tag{4.2}$$

for $i = 1, \ldots, N-1$.

The Lagrange-Euler formulation of Eq. (4.1) yields the following equations of motion:

$$\ddot{\boldsymbol{\theta}} = h(\boldsymbol{\theta}, \dot{\boldsymbol{\theta}}, T) = -\mathcal{I}^{-1}(\boldsymbol{\theta})\left(\mathcal{C}(\boldsymbol{\theta}, \dot{\boldsymbol{\theta}}) + \mathcal{V}(\boldsymbol{\theta}) - \mathcal{F}(T)\right). \tag{4.3}$$

The terms, $\mathcal{I}$, $\mathcal{C}, \mathcal{V}$, and $\mathcal{F}$ in Eq. (4.3) generalize to N links in the following form:

$$\mathcal{I}_{ij} = l^i l^j \cos(\theta^i - \theta^j) \sum_{k=max(i,j)+1}^{N} m_k \tag{4.4}$$

$$\mathcal{C}_i = \sum_{j=1}^{N-1}\left[l^i l^j \dot{\theta}^{j2} \sin(\theta^i - \theta^j) \sum_{k=max(i,j)+1}^{N} m_k\right] \tag{4.5}$$

$$\begin{aligned}
\mathcal{V}_1 &= gl^1 \sin(\theta^1) \sum_{k=2}^{N} m_k \\
&\quad + 2\frac{EI_2}{\bar{\ell}_2} \tan\left(\frac{\theta^1 - \theta^2}{2}\right) \sec^2\left(\frac{\theta^2 - \theta^2}{2}\right) \\
\mathcal{V}_i &= gl^i \sin(\theta^i) \sum_{k=i+1}^{N} m_k \\
&\quad - 2\frac{EI_i}{\bar{\ell}_i} \tan\left(\frac{\theta^{i-1} - \theta^i}{2}\right) \sec^2\left(\frac{\theta^{i-1} - \theta^i}{2}\right) \\
&\quad + 2\frac{EI_{i+1}}{\bar{\ell}_{i+1}} \tan\left(\frac{\theta^i - \theta^{i+1}}{2}\right) \sec^2\left(\frac{\theta^i - \theta^{i+1}}{2}\right) \\
\mathcal{V}_{N-1} &= gl^{N-1} \sin(\theta^{N-1}) \sum_{k=N}^{N} m_k \\
&\quad - 2\frac{EI_{N-1}}{\bar{\ell}_{N-1}} \tan\left(\frac{\theta^{N-2} - \theta^{N-1}}{2}\right) \sec^2\left(\frac{\theta^{N-2} - \theta^{N-1}}{2}\right)
\end{aligned} \tag{4.6}$$

and

$$\mathcal{F} = \begin{bmatrix} T & \dots & 0 \end{bmatrix}^T \tag{4.7}$$

where T is the torque input at the base of the pendulum. Let $\boldsymbol{q}_\theta = \begin{bmatrix} \boldsymbol{\theta} & \dot{\boldsymbol{\theta}} \end{bmatrix}^T$. The state-space representation of the inextensible pendulum dynamics is

$$\dot{\boldsymbol{q}}_\theta = f(\boldsymbol{\theta}, \dot{\boldsymbol{\theta}}, T) = \begin{bmatrix} \dot{\boldsymbol{\theta}} \\ \\ h(\boldsymbol{\theta}, \dot{\boldsymbol{\theta}}, T) \end{bmatrix}, \tag{4.8}$$

where $h(\boldsymbol{\theta}, \dot{\boldsymbol{\theta}}, T)$ is from Eq. (4.3).

4.2.2 Linear control design

For the purpose of stabilizing the up equilibrium, Eq. (4.8) is linearized about $\boldsymbol{q}_\theta^* = (\theta_i, \dot{\theta}_i) = (\pi, 0)$ for all i and $T^* = 0$. Define the coordinate transformation $\boldsymbol{z} = \boldsymbol{q}_\theta - \boldsymbol{q}_\theta^*$

and $u = T - T^*$. Linearization about the up equilibrium yields

$$\dot{\boldsymbol{z}} = A\boldsymbol{z} + Bu \tag{4.9}$$

where $A = \frac{\partial f}{\partial \boldsymbol{q}_\theta}\Big|_{(\boldsymbol{q}_\theta^*, T^*)}$ and $B = \frac{\partial f}{\partial T}\Big|_{(\boldsymbol{q}_\theta^*, T^*)}$ are

$$A = \begin{bmatrix} 0_{N-1\times N-1} & I_{N-1\times N-1} \\ \dfrac{EI}{ml^3}A_b + \dfrac{g}{l}A_g & 0_{N-1\times N-1} \end{bmatrix} \text{ and } B = \begin{bmatrix} 0_{N-1\times 1} \\ \frac{1}{ml^2} \\ -\frac{1}{ml^2} \\ 0_{N-3\times 1} \end{bmatrix}, \tag{4.10}$$

with banded matrices

$$A_b = \begin{bmatrix} -2 & 3 & -1 & 0 & \cdots & & 0 \\ 3 & -6 & 4 & -1 & 0 & & \\ -1 & 4 & -6 & 4 & -1 & 0 & \vdots \\ 0 & \ddots & \ddots & \ddots & \ddots & \ddots & 0 \\ \vdots & 0 & -1 & 4 & -6 & 4 & -1 \\ & & 0 & -1 & 4 & -6 & 3 \\ 0 & & \cdots & 0 & -1 & 5 & -4 \end{bmatrix} \tag{4.11}$$

and

$$A_g = \begin{bmatrix} a_1 & b_1 & 0 & 0 \\ c_1 & \ddots & \ddots & 0 \\ 0 & \ddots & \ddots & b_{N-2} \\ 0 & 0 & c_{N-2} & a_{N-1} \end{bmatrix}, \tag{4.12}$$

having entries $a_1 = N - \frac{3}{2}$, $a_{N-1} = \frac{3}{2}$, $a_i = 2(N-1-i)+1$ for $i = 2, .., N-2$; $b_i = i - N + \frac{3}{2}$; and $c_i = i - N + \frac{1}{2}$, for $i = 1, ..., N-2$.

The rows of matrix A_b represent the forces due to bending take the form of finite difference coefficients for the fourth spatial derivative, such that the linearized system may be considered a spatial discretization of the linear Euler-Bernoulli model for deflection of a beam [29]. The resulting system must satisfy the controllability rank condition $rank([BABA^2B \dots A^{N-1}B]) = N$ for the feedback control laws to stabilize the pendulum.

The resulting linearized model, Eq. (4.9), is used to design a Linear Quadratic Regulator (LQR). The LQR control design seeks to minimize the cost function [30]

$$J = \int_0^\infty \left(\boldsymbol{z}^T Q \boldsymbol{z} + u^T R u \right) dt, \tag{4.13}$$

where Q and R are weighting matrices on the state and input, respectively. The feedback control law that minimizes J is $u = -Kx$, where $K = R^{-1} B^T P$. The matrix P is found by solving the continuous time algebraic Riccati equation [30]. In practice, the state feedback gain matrix K is calculated using the Matlab function `lqr`, with

$$Q = \begin{bmatrix} Q_\theta I_{N-1 \times N-1} & 0_{N-1 \times N-1} \\ 0_{N-1 \times N-1} & Q_{\dot{\theta}} I_{N-1 \times N-1} \end{bmatrix}, \tag{4.14}$$

where $Q_\theta = 100$, $Q_{\dot{\theta}} = 0.01$, and $R = 1$.

4.2.3 Swing-up and hybrid control design

An open-loop swing-up controller drives the state of the pendulum to the effective region of the LQR controller. The swing-up controller simulates the zero-input response of a rigid pendulum from the horizontal initial conditions. The natural frequency $\omega = \sqrt{\frac{g}{L_{tot}}}$ is used as the driving frequency for the swing-up controller

$$T = \mathcal{A}\cos(\omega t), \tag{4.15}$$

where $\mathcal{A} = 0.025$ is the amplitude of the swing-up input. The LQR controller activates when the base edge is within ±60° of the up equilibrium.

The problem of stabilizing an inverted flexible pendulum becomes more challenging when the rod is itself inherently unstable. At certain points in parameter space, the rod is subject to a phenomena known as self-buckling, i.e., when it fails to stand under its own weight with no other loads applied. A fixed-free vertical column with a square cross section, density ρ, Young's modulus E, and height h_c, will buckle at [31]

$$w_{crit} = \sqrt{\frac{16h_c^3}{3B^2}\frac{\rho g}{E}} \tag{4.16}$$

where g is the acceleration due to gravity and B is the first zero of the Bessel function of the first kind of order -1/3. The analytical buckling expression Eq. (4.16) predicts self buckling for a critical width of $w_{crit} = 0.78$ [cm]. (PDER simulation results with for $N = 7$ show that buckling occurs for width less than $w_{crit} \approx 0.81$ [cm].)

Fig. 4.3 shows the pendulum at various times during swing up and stabilization. The simulations are performed using the entire PDER model, while only the controller assumes the behavior of the inextensible linearized system. The pendulum is in the swing-up stage from $t = 0$ to $t \approx 0.75$. The state feedback controller successfully stabilizes the simulated pendulum of $N = 7$ nodes at the up equilibrium and stabilizes some rods that would buckle under zero input. Fig. 4.4 shows that for rods of $w \gtrsim 0.5$ [cm] the state error converges to zero as the up equilibrium is stabilized.

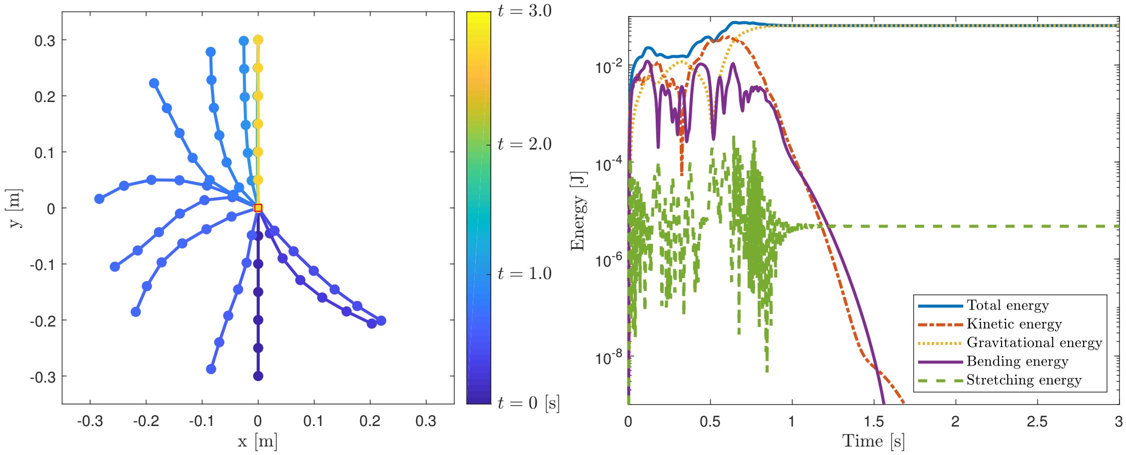

Figure 4.3: Simulation of a rod with $w = 0.7$ [cm] and time step $\Delta t = 1 \times 10^{-4}$ [s] using a state feedback hybrid control design.

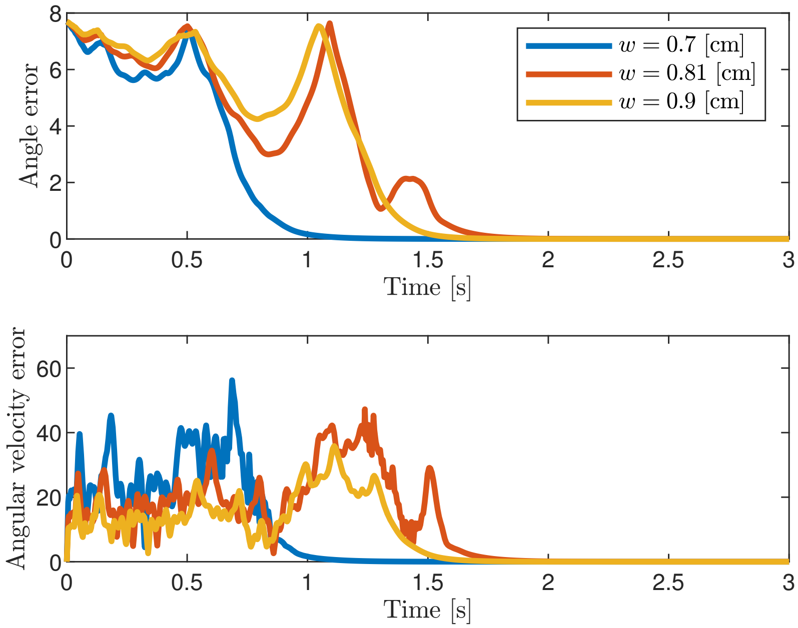

Figure 4.4: The state-feedback control performance of various rods with same initial conditions $(\theta_i, \dot{\theta}_i) = (0, 0)$ for all i. The rod of $w = 0.9$ [cm] is above the buckling width, the rod of width $w = 0.81$ [cm] is at the critical buckling width, and the rod of width $w = 0.7$ [cm] is below the buckling width i.e., it buckles if the base is held fixed.

4.3 Observer-based feedback hybrid control

In practice it is unlikely to have perfect knowledge of the state of the system and more likely to be reliant on information from sensors. Assume a linear output $\boldsymbol{y} = C\boldsymbol{z}$. The filtered sensor data, in conjunction with the model of the system, yields an estimate of the state using a Luenberger observer [30]:

$$\dot{\hat{\boldsymbol{z}}} = A\hat{\boldsymbol{z}} + Bu + L(\boldsymbol{y} - \hat{\boldsymbol{y}}) \tag{4.17}$$

where $\hat{\boldsymbol{z}}$ is the estimated state, $\hat{\boldsymbol{y}} = C\hat{\boldsymbol{z}}$ is the estimated output and L is the observer gain matrix such that $A - LC$ is Hurwitz, i.e. that the eigenvalues fall in the left half of the imaginary plane. The observer gain matrix L is chosen optimally using the Matlab function `kalman` and the values $Q_n = 0.001$ and $R_n = I_{2\times 2}$. The C matrix used to design the observer assumes measurements of only the angle, and angular velocity of the base of the rod, i.e,

$$C = \begin{bmatrix} 1 & 0 & \cdots & 0 & 0 & 0 & \cdots & 0 \\ 0 & 0 & \cdots & 0 & 1 & 0 & \cdots & 0 \end{bmatrix}, \tag{4.18}$$

where the middle entry is centered at the N^{th} column. (The (A, C) pair is observable.)

Let $\boldsymbol{e} = \boldsymbol{z} - \hat{\boldsymbol{z}}$. Implementing the observer, Eq. (4.17), for the linearized state-space system, Eq. (4.8), yields

$$\begin{bmatrix} \dot{\boldsymbol{z}} \\ \dot{\boldsymbol{e}} \end{bmatrix} = \begin{bmatrix} A - BK & BK \\ 0 & A - LC \end{bmatrix} \begin{bmatrix} \boldsymbol{z} \\ \boldsymbol{e} \end{bmatrix}. \tag{4.19}$$

which is Hurwitz as long as $A - BK$ and $A - LC$ are Hurwitz. Fig. 4.5 shows the output-feedback hybrid controller stabilizing the up equilibrium of the PDER simulation.

Fig. 4.6 shows the estimation error $\boldsymbol{e}$ for rods of varying widths. (The observer activates when the base edge is within $\pm 60^\circ$ of the up equilibrium, using the initial estimate $(\theta_i, \dot{\theta}_i) = (\theta_1, \dot{\theta}_1)$ for all i). The simulations are performed using the entire PDER model, while only the controller assumes the behavior of the inextensible linearized system. The estimated state converges to the state of the system sufficiently fast to stabilize the up equilibrium. The nonlinear behavior of the model causes the linear observer to quickly converge near the up equilibrium and then diverge as the pendulum overshoots the up equilibrium. This behavior causes the sequential bumps in Fig. 4.6 most notable in the angle error of the $w = 0.81$ [cm] rod at $t > 1.25$ [s].

4.4 Discussion

This chapter provides a state-space description of a flexible pendulum using a planar discrete elastic rod. State-feedback and output-feedback hybrid controllers stabilize the up equilibrium with measurements taken only at the base of the rod. Simulations suggest that the state-feedback hybrid control and output-feedback hybrid control designs are successful at swinging up and stabilizing the up equilibrium, even for some rods that would otherwise buckle. Future work would seek to extend the result so that the control design can accommodate a PDER simulation that exceeds the number of nodes in the control model; the current implementation fails if the PDER simulation is higher fidelity than the model.

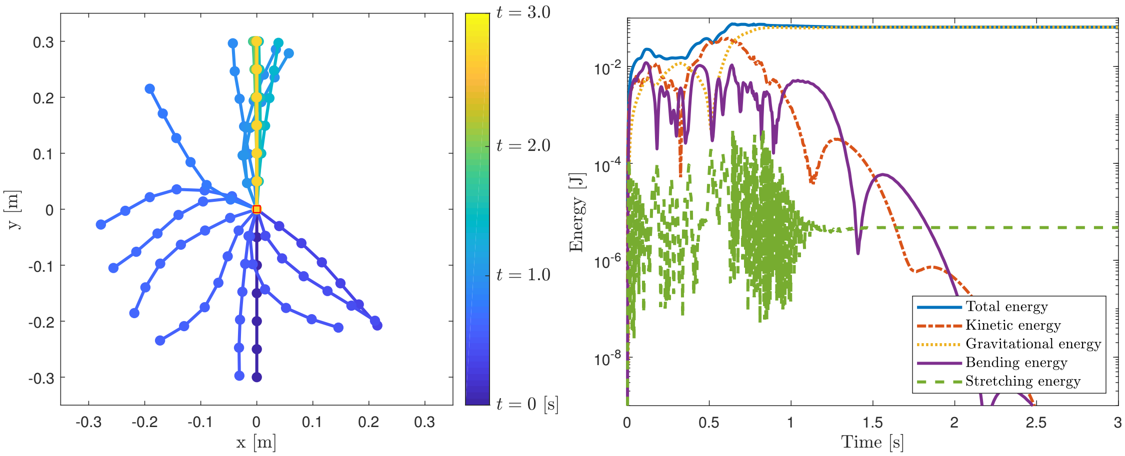

Figure 4.5: Simulation of a rod with $w = 0.7$ [cm] and time step $\Delta t = 1 \times 10^{-4}$ [s] using a output-feedback hybrid control design.

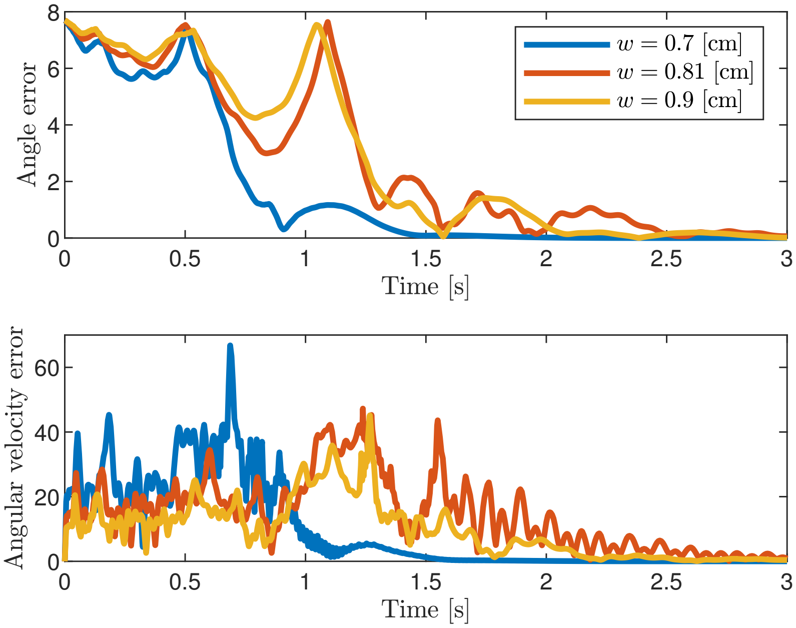

Figure 4.6: Output-feedback control performance of various rods with the initial conditions $(\theta_i, \dot{\theta}_i) = (0, 0)$ for all i.

Chapter 5: Conclusion

In the continued effort to improve and optimize the performance of man-made designs, this thesis turns towards the investigation of modeling and control of bio-inspired flexible structures. Many animals are capable of performing complicated tasks through the exploitation of soft structures. Soft structures are highly versatile and are a growing area of interest in robotics because they can have decreased weight, size, and mechanical complexity than more traditional rigid robotics [2]. However, flexible systems are challenging to model because they may be highly nonlinear, have infinite degrees of freedom, and are generally described by partial differential equations [5]. This structural complexity, coupled with the complexity of interacting with dynamic environments, such as an ambient fluid, make the modeling and control of flexible manipulators a rich problem to be solved.

5.1 Summary of contributions

This work is the first that I am aware of to apply the Improved Lighthill model (ILM) of hydrodynamic forces to study the propulsion thrust of a flexible airfoil modeled using discrete elastic rods. Experiments are performed to measure the thrust produced by pitching rigid and flexible airfoils around the quarter chord in water at varying amplitudes and frequencies. Validation of PDER numerical modeling is performed using a molded silicone rubber airfoil undergoing periodic deformations in air. Experiments suggest that higher thrust is achieved in water by oscillating flexible airfoils instead of a rigid foil of the same geometry at the same frequency and amplitude. The experimental thrust produced by both the rigid, and flexible foil increase with Strouhal number. The ILM is used to attempt to predict fluid forces on a rigid and flexible airfoil. For both the rigid and flexible foil, the ILM does not provide good agreement with the experimental data under the operating conditions in this work.

This work also provides a state-space description of a flexible pendulum with torque input using planar discrete elastic rod theory, a state-feedback hybrid control design for balancing the inverted flexible pendulum and a dynamic output-feedback hybrid control design using a linear observer that relies only on measurements of the position and angular velocity of the base of the rod. Performance of the control strategy for stabilizing a PDER pendulum is illustrated using numerical simulations. The pendulum parameters are chosen to satisfy the conventional self-buckling condition; simulations suggest that the feedback control design balances some rods that buckle under zero input.

5.2 Suggestions for future work

In future work we would suggest validating the thrust measurements against a more simplified hydrodynamic forces model that doesn't assume attached flow. Acceleration of fluid along the length of a submerged is one of the core mechanisms of thrust production in LAEBT and subsequently the ILM. The geometry of the airfoil used in this work may not have allowed for an adequate amount of attached flow which accelerates the fluid along the length of the airfoil and into the wake. We would also seek to include a propulsive efficiency metric as in [7].

Regarding the control of soft structures, we would suggest preparing an experimental testbed for the inverted flexible pendulum to validate the stability results suggested by simulation. We would also seek to extend the stability results of the inverted pendulum such that the control design can accommodate a PDER simulation that exceeds the number of nodes in the control model; the current implementation fails if the PDER simulation is higher fidelity than the model. Additionally, we would seek to study the controllability of the linearized pendulum model as a function of geometric and structural parameters such as aspect ratio and flexural stiffness.

Appendix A: Camera calibration

The procedure used for this work follows the camera calibration method in the Matlab computer vision toolbox [32]. The camera is calibrated for intrinsic parameters in air and in water before calibrating the extrinsic parameters before each experiment.

A.1 Intrinsic parameters

The underwater camera intrinsic parameters were estimated by taking numerous images containing a checkerboard pattern of a known dimension. Enough images were taken such that the field of view of the camera was covered completely. This intrinsic calibration was done with the camera in air as well as submerged in water. The checkerboard pattern used for calibration was 10 by 7 cells. The calibration algorithm locates the interior vertices of the pattern, which results in 54 nodes being identified. All images were taken approximately 20 cm from the checkerboard pattern with each cell measuring 7.34 × 7.34 mm. The intrinsic parameters calculated for the camera in air and water are given in Table A.1. The intrinsic parameters form the intrinsic matrix, K, given in [32] by

$$K = \begin{bmatrix} f_x & 0 & 0 \\ s & f_y & 0 \\ c_x & c_y & 1 \end{bmatrix} \tag{A.1}$$

where $[f_x \quad f_y]$ is the focal length, $[c_x \quad c_y]$ is the principle point, and s is the skew. The intrinsic parameters are then used to correct for distortions before calculating extrinsic

Table A.1: Camera parameters

Name	Air	Water	Units
# of Images	30	25	[ ]
Focal Length	[801.17 789.65]	[1087.2 1082.6]	[pixels]
Principle Point	[605.94 358.89]	[614.88 336.99]	[pixels]
Skew	0	0	[%]
Radial Distortion	[−0.2770 0.0660]	[−0.1454 − 0.0514]	[%]
Tangential Distortion	[0 0]	[0 0]	[%]
Mean Re-projection Error	0.8672	1.4340	[pixels]

parameters and before performing measurements within an image. The effect of correcting the distortion caused by the camera can be seen in Fig. A.1.

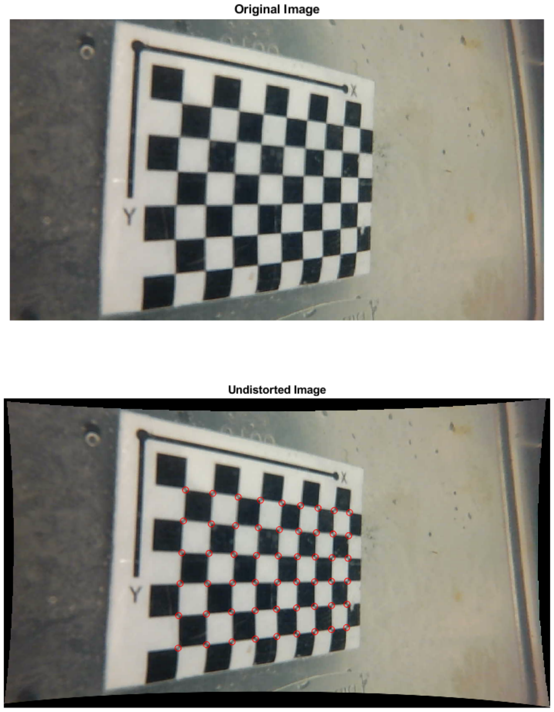

Figure A.1: Image before and after correcting for camera distortion

A.2 Extrinsic parameters

Once the intrinsic parameters have been calculated for the camera in air and water, the extrinsic parameters are found. The extrinsic parameters correspond to the relative location of the camera to the plane that we intend to image. The extrinsic parameters were found by affixing the checkerboard pattern to the base of the airfoil, capturing an image and calculating the translation and rotation of the camera. The transformation from the checkerboard frame to the world frame is given in [32] by

$$s\,[x \quad y \quad 1] = [X \quad Y \quad Z \quad 1] \begin{bmatrix} R \\ \\ t \end{bmatrix} K \tag{A.2}$$

where $[x \quad y]$ are the image points, $[X \quad Y \quad Z]$ are the world coordinates in the checkerboard frame, R is the rotation matrix, t is the translation vector and K is the intrinsic matrix. Due to the fact that the camera is mounted on a swivel and subject to small changes in position between experiments, these parameters are recalculated before each experiment to ensure proper calibration.

Appendix B: Data collection routine

Algorithm 1 Data Collection

```
Define Test Matrix;
Open Communication with NI Board;
Define Sample Rate and Test Duration;
Connect to Arduino;
for Test Matrix do
    Perform Tare;
    Send Command String;
    while Begin flag = false do
        if Arduino Begin Test then
            Start National instruments clock;
            Start Matlab clock;
        else
            Begin flag = false;
        end if
    end while
    while Current Time < Test Duration do
        Collect image;
        Read servo angle from Arduino;
        Collect Matlab timestamp;
    end while
    Collect load data with timestamps from National Instruments board;
    Store images, load data, servo angle, and test conditions in structure;
end for
```

Bibliography

[1] S. Kim, C. Laschi, and B. Trimmer. Soft robotics: a bioinspired evolution in robotics. *Trends in biotechnology*, 31(5):287–294, 2013.

[2] D. Sun and J. K. Mills. Control of a rotating cantilever beam using a torque actuator and a distributed piezoelectric polymer actuator. *Applied Acoustics*, 63(8):885–899, 2002.

[3] K. C. Galloway, K. P. Becker, B. Phillips, J. Kirby, S. Licht, D. Tchernov, R. J. Wood, and D. F. Gruber. Soft robotic grippers for biological sampling on deep reefs. *Soft Robotics*, 3(1):23–33, 2016.

[4] F. Zhang, P. Washington, and D. A. Paley. A flexible, reaction-wheel-driven fish robot: Flow sensing and flow-relative control. In *Proc. American Control Conference*, pages 1221–1226, 2016.

[5] S. Kawaji and K. Kanazawa. Control of double inverted pendulum with elastic joint. In *Proc. IEEE/RSJ International Workshop on Intelligent Robots and Systems*, pages 946–951, 1991.

[6] R. Mittal, H. Dong, M. Bozkurttas, G. V. Lauder, and P. Madden. Locomotion with flexible propulsors: II. computational modeling of pectoral fin swimming in sunfish. *Bioinspiration & biomimetics*, 1(4):S35, 2006.

[7] J. H. J. Buchholz and A. J. Smits. The wake structure and thrust performance of a rigid low-aspect-ratio pitching panel. *Journal of fluid mechanics*, 603:331–365, 2008.

[8] H. Dai, H. Luo, P. J. S. A. Ferriera de Sousa, and J. F. Doyle. Thrust performance of a flexible low-aspect-ratio pitching plate. *Physics of Fluids*, 24(10):101903, 2012.

[9] D. B. Quinn, G. V. Lauder, and A. J. Smits. Scaling the propulsive performance of heaving flexible panels. *Journal of fluid mechanics*, 738:250–267, 2014.

[10] M. J. Lighthill. Large-amplitude elongated-body theory of fish locomotion. *Proceedings of the Royal Society of London. Series B. Biological Sciences*, 179(1055):125–138, 1971.

[11] M. Porez, F. Boyer, and A. J. Ijspeert. Improved lighthill fish swimming model for bio-inspired robots: Modeling, computational aspects and experimental comparisons. *The International Journal of Robotics Research*, 33(10):1322–1341, 2014.

[12] S. K. Dwivedy and P. Eberhard. Dynamic analysis of flexible manipulators, a literature review. *Mechanism and Machine Theory*, 41(7):749–777, 2006.

[13] N. N. Goldberg, X. Huang, C. Majidi, A. Novelia, O. M. O'Reilly, D. A. Paley, and W. L. Scott. On planar discrete elastic rod models for the locomotion of soft robots. *Soft robotics*, 2019.

[14] S. K. Gorade, P. S. Gandhi, and S. R. Kurode. Modeling and output feedback control of flexible inverted pendulum on cart. In *Proc. International Conference on Power and Advanced Control Engineering*, pages 436–440, 2015.

[15] M. V. Trivedi, R. N. Banavar, and B. M. Maschke. Modeling of hybrid lumped-distributed parameter mechanical systems with multiple equilibria. In *Proc. 18th IFAC World Congress, Milano, Italy*, volume 18, pages 7696–7701, 2011.

[16] O. Patil and P. Gandhi. On the dynamics and multiple equilibria of an inverted flexible pendulum with tip mass on a cart. *Journal of Dynamic Systems, Measurement, and Control*, 136(4):041017, 2014.

[17] C. Xu and X. Yu. Mathematical modeling of elastic inverted pendulum control system. *Journal of Control theory and applications*, 2(3):281–282, 2004.

[18] K. A. Kong. Fuzzy logic pd control of a non-linear inverted flexible pendulum. 2009.

[19] J. Tang and G. Ren. Modeling and simulation of a flexible inverted pendulum system. *Tsinghua Science & Technology*, 14(S2):22–26, 2009.

[20] A. Singla. Vibration suppression of a cart-flexible pole system using a hybrid controller. In *Proc. 1st International and 16th National Conference on Machines and Mechanisms, India*, pages 375–382, 2013.

[21] M. K. Jawed, A. Novelia, and O. M. O'Reilly. *A Primer on the Kinematics of Discrete Elastic Rods*. Springer, 2018.

[22] M. Bergou, M. Wardetzky, S. Robinson, B. Audoly, and E. Grinspun. Discrete elastic rods. *ACM Transactions on Graphics*, 27(3):63, 2008.

[23] G. I. Taylor. Analysis of the swimming of long and narrow animals. *Proceedings of the Royal Society of London. Series A. Mathematical and Physical Sciences*, 214(1117):158–183, 1952.

[24] J. Gray. Studies in animal locomotion: I. the movement of fish with special reference to the eel. *Journal of experimental biology*, 10(1):88–104, 1933.

[25] F. Boyer, M. Porez, A. Leroyer, and M. Visonneau. Fast dynamics of an eel-like robot comparisons with navier-stokes simulations. *IEEE Transactions on Robotics*, 24(6):1274–1288, 2008.

[26] S. F. Hoerner. Fluid-dynamic drag. *Hoerner Fluid Dynamics*, 1965.

[27] O. A. Shergold, N. A. Fleck, and D. Radford. The uniaxial stress versus strain response of pig skin and silicone rubber at low and high strain rates. *International Journal of Impact Engineering*, 32(9):1384–1402, 2006.

[28] M. J. McHenry, C. A. Pell, and J. H. Long. Mechanical control of swimming speed: stiffness and axial wave form in undulating fish models. *Journal of Experimental Biology*, 198(11):2293–2305, 1995.

[29] J. M. Gere and S. P. Timoshenko. *Mechanics of materials.* PWS-KENT Publishing Company, 1997.

[30] C. Chen. *Linear system theory and design.* Oxford University Press, 1998.

[31] A. G. Greenhill. Determination of the greatest height consistent with stability that a vertical pole or mast can be made, and of the greatest height to which a tree of given proportions can grow. *Proc. Cambridge Philosophical Society*, 4:65–73, 1881.

[32] The MathWorks Inc. *Computer Vision Toolbox: For Use with MATLAB;User's Guide.* The MathWorks Inc., 2019.